



How does the North Pacific Meridional Mode affect the Indian Ocean Dipole?

Xin Cheng^{1,3} · Shangfeng Chen^{1,3} · Wen Chen^{2,4} · Peng Hu^{2,4} · Zhencai Du¹ · Xiaoqing Lan¹ · Yuqiong Zheng^{2,4}

Received: 27 July 2023 / Accepted: 1 December 2023 / Published online: 5 January 2024
© The Author(s), under exclusive licence to Springer-Verlag GmbH Germany, part of Springer Nature 2024

Abstract

This study reveals a strong relationship between the North Pacific Meridional Mode (PMM) in boreal spring and the Indian Ocean Dipole (IOD) in following autumn. A positive spring PMM tends to be followed by a positive IOD and vice versa. The mechanism for the influence of the PMM on the IOD is then investigated. Positive spring PMM-related cyclonic and SST warming anomalies over the subtropical North Pacific propagate southward to the equatorial central Pacific in the following summer via wind–evaporation–SST feedback. SST warming and enhanced atmospheric heating in summer in the equatorial central Pacific induce an anomalous Walker circulation with ascending anomalies over the tropical central Pacific and descending anomalies over the Maritime Continent. The descending anomalies over the Maritime Continent result in southeasterly wind anomalies off the west coast of Sumatra, which lead to cold SST anomalies in the southeastern tropical Indian Ocean via modulating surface heat flux and upwelling of cold water. The associated increase in zonal SST gradient in the tropical Indian Ocean leads to low-level easterly wind anomalies and contributes to warm SST anomalies in the western tropical Indian Ocean via oceanic dynamic process. The warm and cold SST anomalies in the tropical western and southeastern Indian Ocean further develop to an IOD event in the following autumn via a positive air–sea interaction. The above process for the PMM influence on IOD can be simulated in the long historical simulations of coupled climate models. This study suggests that the spring PMM is a potential precursor for the occurrence of IOD event in the following autumn.

Keywords Indian Ocean Dipole · Pacific Meridional mode · Air–sea interaction

1 Introduction

The Indian Ocean Dipole (IOD) is a prominent air–sea interaction mode in the tropical Indian Ocean (IO) that usually peaks in the boreal autumn and is featured by a west–east sea surface temperature (SST) gradient and zonal wind anomalies along the equatorial IO (Saji et al. 1999; Webster

et al. 1999). The occurrences of IOD events have substantial global impacts by altering ocean–atmosphere circulations, particularly in Australia, India, Africa and East Asia (Ashok et al. 2001; Yamagata et al. 2004; Terray et al. 2007; Cai et al. 2011; Qiu et al. 2014; Chen et al. 2018; Zhang et al. 2019; Zhang et al. 2022a, b, c; Wahiduzzaman et al. 2022; Zhang et al. 2023). Due to its large climatic and economic impacts, a comprehensive study of the formation and development mechanism of IOD is of critical significance.

Local air–sea interaction and oceanic dynamics within the tropical IO are important for the occurrence and development of IOD events (Behera et al. 1999; Yang et al. 2015; Wang et al. 2016; Liu et al. 2017; Lu et al. 2018; Aparna and Girishkumar 2022). For example, initial SST anomalies in the tropical eastern IO would alter the zonal SST gradient in the tropical IO and induce surface zonal wind anomalies. These surface zonal wind anomalies contribute to IOD development through Bjerknes-like positive air–sea feedback and surface–subsurface interaction (Wang et al. 2016). In addition to the local process within the IO, studies have suggested

✉ Shangfeng Chen
chenshangfeng@mail.iap.ac.cn

¹ Center for Monsoon System Research, Institute of Atmospheric Physics, Chinese Academy of Sciences, Beijing 100029, China

² Yunnan Key Laboratory of Meteorological Disasters and Climate Resources in the Greater Mekong Subregion, Yunnan University, Kunming 650091, China

³ College of Earth and Planetary Sciences, University of Chinese Academy of Sciences, Beijing 100049, China

⁴ Department of Atmospheric Sciences, Yunnan University, Kunming 650500, China

that external forcing outside the IO also plays a critical role in modulating the occurrence of IOD. For example, studies suggested that SST anomalies in the tropical Pacific associated with the El Niño and Southern Oscillation (ENSO) could strongly influence the IOD through modulating the tropical Walker circulation (Xie et al. 2002; Annamalai et al. 2003; Fischer et al. 2005; Behera et al. 2006; Roxy et al. 2011; Huang et al. 2022). With the frequent occurrence of Central Pacific (CP) El Niño events after the early-1990s, many studies have examined the complicated CP ENSO-IOD relationships (Ashok et al. 2007; Izumo et al. 2010, 2014; Liang 2014; Krishnaswamy et al. 2015; Yeh et al. 2015; Strnad et al. 2022). In addition to the ENSO, the evolution of IOD can also be modulated by other tropical climate systems, including the tropical cyclone over the Bay of Bengal (Francis et al. 2007), SST anomalies in the tropical Atlantic (Wang et al. 2009; Zhang et al. 2022a, b), and the tropical cross-equatorial flow in Indonesia (Song and Gordon 2004).

The influence of climate systems outside the tropics on the IOD is less investigated. The North Pacific Meridional mode (PMM), the leading atmosphere–ocean coupled variability over the subtropical northeast Pacific, is an important precursor for the occurrence of ENSO (Chiang and Vimont 2004; Liu et al. 2019; Larson and Kirtman 2014; Lin et al. 2015; Min et al. 2017; Zheng et al. 2021a, b; Fan et al. 2021; Richter et al. 2022). The PMM-induced SST, precipitation and atmospheric anomalies over the subtropical North Pacific could propagate southward to the tropical Pacific via the wind–evaporation–SST (WES) feedback, which further exert impacts on the ENSO development via tropical dynamical processes (Xie and Philander 1994; Yu et al. 2010; Amaya 2019; Lin et al. 2015; Zheng et al. 2023). In addition to the WES feedback, studies have indicated the PMM can also impact the ENSO development via the oceanic process (Yu and Kim 2010; Wang and Wang 2013; Wang et al. 2018; Chen et al. 2023). Particularly, the PMM-related surface wind stress anomalies over the subtropical North Pacific could induce surface wind curl anomalies over the tropical central Pacific. These could induce sub-surface ocean temperature anomalies over the tropical central Pacific via Ekman pumping and meridional oceanic currents, which further impact following winter ENSO development (Anderson and Karspeck 2013; Anderson and Perez 2015; Wang et al. 2019; Guan et al. 2023). Since PMM could impact the tropical Pacific SST, and the IOD may be affected by the tropical Pacific SST, we speculate that the PMM may be able to modulate the occurrence and development of the IOD. In this study, we present evidence to show that this is indeed the case. We show that the spring PMM is significantly related to the following autumn IOD occurrence. We then examine the physical processes, including the relative roles of ocean dynamics and atmospheric thermal forcing, involved in the PMM-IOD linkage.

The rest of this paper is organized as follows. Section 2 present the data and methodology. The lead-lag relationship between the PMM and IOD is examined in Sect. 3. Section 4 investigates the physical process for the impact of the PMM on the IOD. Section 5 summarizes our findings.

2 Data and methods

2.1 Data

Monthly mean SST data were obtained from the National Oceanic and Atmospheric Administration (NOAA) Extended Reconstructed SST, version 5 (ERSSTv5) (Huang et al. 2017; downloaded from <https://www.esrl.noaa.gov/psd/data/gridded/data.noaa.ersst.v5.html>). This SST dataset spans from January 1854 to the present and has a horizontal resolution of $2^\circ \times 2^\circ$. Monthly winds, precipitation rate, and surface heat fluxes are obtained from the National Centers for Environmental Prediction and the National Center for Atmospheric Research reanalysis (NCEP-NCAR) (Kalnay et al. 1996), starting in January 1948. We also use the monthly precipitation data from the Global Precipitation Climatology Project (GPCP) (Adler et al. 2003) with a horizontal resolution of $1.25^\circ \times 1.25^\circ$ and from the CPC Merged Analysis of Precipitation (CMAP) with a horizontal resolution of $2.5^\circ \times 2.5^\circ$ (Xie and Arkin 1996) to confirm the results from the NCEP-NCAR. The net surface heat flux is the sum of the surface sensible and latent heat fluxes, and the net surface shortwave and longwave radiation. To calculate the mixed-layer heat budget equation, we obtained the monthly oceanic variables including potential temperature, zonal current, meridional current, vertical current, and ocean mixed layer depth from the Global Ocean Assimilation System (GODAS) (Behringer and Xue 2004). These three-dimensional currents, potential temperature, and ocean mixed layer depth all have a zonal resolution of 1° and meridional resolution of $1/3^\circ$ and have 40 vertical levels in the upper 200 m from 1980 to 2021 (Behringer and Xue 2004).

In addition, we use the historical simulation outputs from 38 coupled models participated in the CMIP6. Detailed information of these 38 models is provided in Table 1. A 9-year high pass Lanczos filter was used to extract interannual components of all data (Duchon 1979). Using a 7-year or 11-year high pass filter gives similar results (not shown).

2.2 Methods

The dipole mode index (DMI) is employed to measure IOD variability (Saji et al. 1999), which is calculated as the area-averaged SST difference between the tropical western Indian Ocean (WTIO; $10^\circ \text{S}–10^\circ \text{N}$, $50^\circ–70^\circ \text{E}$) and the tropical

Table 1 Information about the 38 models in CMIP6

Model Name	Modeling centers	Resolution (lat × lon)
ACCESS-CM2	CSIRO-ARCCSS (Commonwealth Scientific and Industrial Research Organization, Australian Research Council Centre of Excellence for Climate System Science)	144 × 192
ACCESS-ESM1-5	CSIRO (Commonwealth Scientific and Industrial Research Organization)	145 × 192
AWI-CM-1-1-MR	AWI (Alfred Wegener Institute)	192 × 384
BCC-CSM2-MR	BCC (Beijing Climate Center)	160 × 320
CAMS-CSM1-0	CAMS(Chinese Academy of Meteorological Sciences)	160 × 320
CanESM5	CCCMA(Canadian Centre for Climate Modelling and Analysis)	64 × 128
CanESM5-CanOE	CCCMA(Canadian Centre for Climate Modelling and Analysis)	64 × 128
CAMS-CSM1-0	CAMS(Chinese Academy of Meteorological Sciences)	320 × 160
CAS-ESM2-0	CAS(Chinese Academy of Sciences)	128 × 256
CESM2	NCAR (National Center for Atmospheric Research)	192 × 288
CESM2-WACCM	NCAR (National Center for Atmospheric Research)	192 × 288
CIESM	THU (Tsinghua University–Department of Earth System Science)	192 × 288
CMCC-CM2-SR5	CMCC (Centro Euro-Mediterraneo per I Cambiaenti Climatici)	192 × 288
CMCC-ESM2	CMCC (Centro Euro-Mediterraneo per I Cambiaenti Climatici)	192 × 288
CNRM-CM6-1	CNRM-CERFACS (National Center for Meteorological Research, Météo-France and CNRS laboratory, Climate Modeling and Global change)	128 × 256
CNRM-CM6-1-HR	CNRM-CERFACS (National Center for Meteorological Research, Météo-France and CNRS laboratory, Climate Modeling and Global change)	360 × 720
CNRM-ESM2-1	CNRM-CERFACS (National Center for Meteorological Research, Météo-France and CNRS laboratory, Climate Modeling and Global change)	128 × 256
E3SM-1-1	E3SM-Project RUBISCO (Energy Exascale Earth System Model, Reducing Uncertainty in Bio-geochemical Interactions through Synthesis and Computation)	90 × 90
EC-Earth3	EC-Earth-Consortium	256 × 512
EC-Earth3-Veg	EC-Earth-Consortium	256 × 512
EC-Earth3-Veg-LR	EC-Earth-Consortium	160 × 320
FGOALS-f3-L	CAS(Chinese Academy of Sciences)	180 × 360
FGOALS-g3	CAS(Chinese Academy of Sciences)	80 × 180
FIO-ESM-2-0	FIO-QLNM (First Institute of Oceanography (FIO) and Qingdao National Laboratory for Marine Science and Technology (QLNM))	192 × 288
GFDL-CM4	NOAA-GFDL (National Oceanic and Atmospheric Administration, Geophysical Fluid Dynamics Laboratory)	180 × 288
GFDL-ESM4	NOAA-GFDL (National Oceanic and Atmospheric Administration, Geophysical Fluid Dynamics Laboratory)	180 × 288
HadGEM3-GC31-MM	MOHC (Met Office Hadley Centre)	324 × 432
IITM-ESM	CCCR-IITM (Centre for Climate Change Research, Indian Institute of Tropical Meteorology)	94 × 192
INM-CM4-8	INM (Institute of Numerical Mathematics)	120 × 180
INM-CM5-0	INM (Institute of Numerical Mathematics)	120 × 180
IPSL-CM6A-LR	IPSL (Institut Pierre-Simon Laplace)	143 × 144
KACE-1-0-G	NIMS-KMA(National Institute of Meteorological Sciences/Korea Met. Administration)	144 × 192
MCM-UA-1-0	UA (University of Arizona–Department of Geosciences)	80 × 96
MIROC6	MIROC (Atmosphere and Ocean Research Institute (AORI), Centre for Climate System Research-National Institute for Environmental Studies (CCSR-NIES) and Atmosphere and Ocean Research Institute (AORI))	128 × 256
MIROC-ES2L	MIROC (Atmosphere and Ocean Research Institute (AORI), Centre for Climate System Research-National Institute for Environmental Studies (CCSR-NIES) and Atmosphere and Ocean Research Institute (AORI))	64 × 128
MPI-ESM1-2-LR	MPI-M AWI (Max Planck Institute for Meteorology (MPI-M), AWI (Alfred Wegener Institute))	96 × 192
MRI-ESM2-0	MRI (Meteorological Research Institute, Japan)	160 × 320
NESM3	NUIST (Nanjing University of Information Science and Technology)	96 × 192
NorESM2-LM	NCC (Norwegian Climate Centre)	96 × 144

southeastern Indian Ocean (SETIO; 10° S–0°, 90°–110° E). The PMM is represented by the first singular value decomposition mode of SST and surface winds over the region of 21° S–32° N and 175° E–95° W (Chiang and Vimont 2004; Chang et al. 2007; Zheng et al. 2023). The PMM index is defined as the expansion coefficient time series of the SST corresponding to the first SVD mode. Following Chang et al. (2007), the cold tongue SST index (SST anomalies averaged in 6° S–6° N, 180°–90° W) has been linearly removed before the SVD analysis to ensure the independence from the ENSO cycle. The EOF method is also employed to define the PMM index to assess the reliability of the SVD-defined PMM index. As has been demonstrated by Richter et al. (2022), the first EOF mode of SST anomalies over the region of 21° S–32° N and 175° E–95° W after removing the cold tongue index could represent the PMM pattern and the PMM index is defined as the principal component (PC) time series corresponding to the EOF1 (Richter et al. 2022). We use the Niño3.4 index, defined as area-averaged SST anomalies in the region of 5° S–5° N and 170°–120° W, to characterize the ENSO variability (Trenberth 1997; Chen et al. 2014).

Significance levels of the regression and correlation coefficients are assessed using a two-tailed Student’s t test. Due to the potential autocorrelation of the time series, the effective sample size (N^*) was estimated following Bretherton et al. (1999), which is described as follows:

$$N^* = N \times \left(\frac{1 - r_1 r_2}{1 + r_1 r_2} \right), \tag{1}$$

N^* is the effective sample size, N represents the original length of the time series. r_1 and r_2 denote the lag one autocorrelation coefficients of the two-time series involved in the correlation analysis.

We diagnose the mixed layer heat budget to quantitatively examine the process for the formation of the SST anomalies in the tropical IO in association with the PMM (Qu 2003; Santoso et al. 2010; Schiller and Ridgway 2013; Graham et al. 2014; Vijith et al. 2020). Following Vijith et al. (2020), the mixed layer heat budget is expressed as follows:

$$\begin{aligned} \underbrace{\frac{\partial T_a}{\partial t}}_{\text{Tendency}} = & - \underbrace{\left(u_a \frac{\partial T_a}{\partial x} + v_a \frac{\partial T_a}{\partial y} \right)}_{\text{Horizontal advection}} + \underbrace{k_H \left(\frac{\partial^2 T_a}{\partial x^2} + \frac{\partial^2 T_a}{\partial y^2} \right)}_{\text{Horizontal mixing}} - \underbrace{\frac{1}{h} \left[k_Z \frac{\partial T}{\partial z} \right]_{-h}}_{\text{Vertical mixing}} \\ & - \underbrace{\left(\frac{T_a - T_{-h}}{h} \right) \left(\frac{\partial h}{\partial t} + w_{-h} + u_{-h} \frac{\partial h}{\partial x} + v_{-h} \frac{\partial h}{\partial y} \right)}_{\text{Entrainment}} + \underbrace{\frac{q_0 - q_{pen}}{\rho_0 C_p h}}_{\text{Net heat flux}}. \end{aligned} \tag{2}$$

Here, ρ_0 , C_p , and T are the seawater density, ocean heat capacity, and seawater temperature, respectively. h is the temporally and spatially varying mixed layer depth. q_{pen} represents the penetrative loss of shortwave radiation and q_0 is the net surface heat flux. k_H and k_Z are the horizontal and vertical eddy diffusivities, respectively. T_a , u_a and v_a are the

vertically averaged oceanic temperature, zonal and meridional current velocities, respectively, in the mixed layer depth. w_{-h} , u_{-h} , v_{-h} , and T_{-h} denote the vertical, zonal, meridional velocity, and oceanic temperature at the base of the mixed layer, respectively. The terms for horizontal mixing ($k_H \left(\frac{\partial^2 T_a}{\partial x^2} + \frac{\partial^2 T_a}{\partial y^2} \right)$), vertical mixing ($\frac{1}{h} \left[k_Z \frac{\partial T}{\partial z} \right]_{-h}$), and penetrating shortwave radiation (q_{pen}) are much smaller than other terms and are therefore omitted as in previous studies (Graham et al. 2014; Qu 2003; Santoso et al. 2010; Schiller and Ridgway 2013; Vijith et al. 2020). Hence, Eq. (2) can be simplified as follows:

$$\frac{\partial T_a}{\partial t} = -u_a \frac{\partial T_a}{\partial x} - v_a \frac{\partial T_a}{\partial y} - w_e \frac{T_a - T_{-h}}{h} + \frac{q_0}{\rho_0 C_p h} + R \tag{3}$$

$$w_e = \frac{\partial h}{\partial t} + w_{-h} + u_{-h} \frac{\partial h}{\partial x} + v_{-h} \frac{\partial h}{\partial y} \tag{4}$$

$$q_0 = R_s + R_l + S_h + L_h. \tag{5}$$

In Eq. (3), $\frac{\partial T_a}{\partial t}$ denotes oceanic temperature tendency term; $-u_a \frac{\partial T_a}{\partial x} - v_a \frac{\partial T_a}{\partial y}$ is the horizontal advection term; $-w_e \frac{T_a - T_{-h}}{h}$ is the entrainment term; $\frac{q_0}{\rho_0 C_p h}$ represents net heat flux term. R represents residual term, including high frequency eddies, vertical and lateral diffusion, and any spurious numerical diffusion. w_e is the sum of mix layer tendency ($\frac{\partial h}{\partial t}$), lateral induction ($u_{-h} \frac{\partial h}{\partial x} + v_{-h} \frac{\partial h}{\partial y}$), and vertical advection (w_{-h}). q_0 is surface net heat flux (Eq. (5)). All terms on the right-hand side of Eq. (5) are assumed to be positive (negative) if they act to warm (cool) the SST.

Furthermore, a variable (such as T_a) can be decomposed into the sum of the climatological mean state and the anomaly state (i.e., $T_a = \overline{T_a} + T_a'$) according to Graham et al. (2014). Thus, Eq. (3) could be further expressed as follows:

$$\begin{aligned} \frac{\partial T_a'}{\partial t} = & - \left(\frac{\partial T_a'}{\partial x} + u_a' \frac{\partial \overline{T_a}}{\partial x} + u_a' \frac{\partial T_a'}{\partial x} \right) \\ & - \left(\frac{\partial T_a'}{\partial y} + v_a' \frac{\partial \overline{T_a}}{\partial y} + v_a' \frac{\partial T_a'}{\partial y} \right) \\ & - \left(\frac{T_a' - T_{-h}'}{h} + w_e' \frac{\overline{T_a} - \overline{T_{-h}}}{h} + w_e' \frac{T_a' - T_{-h}'}{h} \right) \\ & + \frac{q_0'}{\rho_0 C_p h} + R' \end{aligned} \tag{6}$$

On the right-hand side of Eq. (6), the first three terms consist of three components: the anomalous term due to anomalous temperature and mean flow, the anomalous term due to mean temperature and anomalous flow, and the non-linear term due to anomalous temperature and flow, which

are used to quantitatively investigate different ocean dynamic processes. $-\overline{w_e' \frac{T_a' - T_h'}{h}}$ is the thermocline feedback term; $-\overline{w_e' \frac{T_a' - T_h'}{h}}$ is the Ekman feedback term; $-\overline{u_a' \frac{\partial T_a'}{\partial x}}$ and $-\overline{v_a' \frac{\partial T_a'}{\partial y}}$ represent the zonal and meridional advective feedback terms, respectively; $-\overline{u_a' \frac{\partial T_a'}{\partial x}}$ and $-\overline{v_a' \frac{\partial T_a'}{\partial y}}$ represent the mean flow effect.

3 Linkage between PMM and IOD

The IOD tends to peak in the boreal autumn, when its climate impacts are most pronounced. We therefore examine the lead-lag relationship of the PMM index with the autumn IOD index (Fig. 1a). Here, autumn is the mean of September, October and November (SON). The autumn IOD index has the strongest connection with the PMM index in preceding April, with the correlation between them exceeding the 99% confidence level (Fig. 1a). To exclude the possibility that the close connection between April PMM and autumn IOD is due to the effect of ENSO (Alexander et al. 2002; Fan

et al. 2017; Wang 2019), we have recalculated the lead-lag correlation between the PMM and IOD indices after removing the preceding winter ENSO signal using a linear regression method. It shows that the close relationship between April PMM and autumn IOD still exists after removal of the ENSO signal (Fig. 1a). In the following analysis, the winter ENSO signal has been removed from all the variables to ensure that the results obtained in this study are not due to the ENSO cycle. Further, we have calculated the relationship between the PMM and the IOD under different methods to define PMM (Richter et al. 2022). Particularly, in addition to the traditional SVD method, we also used the EOF method to define the PMM following Richter et al. (2022). The correlation coefficient between the EOF-defined PMM index and the SVD-defined PMM index is as high as 0.9. Furthermore, it is noteworthy that the evolution of the correlation coefficients between the EOF-defined PMM index and the IOD index is basically consistent with that between the traditional SVD-defined PMM index and the IOD index, both with the highest correlation occurring in April (Fig. 1a, b). Hence, this suggests that the results obtained in this study are not sensitive to the method used to define the PMM. Therefore, the PMM index used in subsequent analyses are defined by the traditional SVD method unless otherwise stated. Note that using the MAM-mean PMM index leads to similar results compared to using the April PMM index, but with slightly weaker signals. Therefore, in the rest of this study, the spring PMM refers to the April PMM and the autumn IOD refers to the SON IOD unless otherwise stated.

Normalized time series of the spring PMM index and the autumn IOD index are shown in Fig. 1c. The correlation coefficient between the two time series is 0.32 over 1958–2021 which exceeds the 95% confidence level. We defined a positive (negative) PMM event when the spring PMM index is greater (smaller) than one (minus one) standard deviation. There are 9 positive PMM events in the period of 1958–2021, including 1959, 1972, 1982, 1986, 1997, 2002, 2010, 2015 and 2018, and 9 negative PMM events, including 1960, 1975, 1984, 1998, 2001, 2008, 2012, 2017 and 2021. Similarly, positive (negative) IOD years are selected when the normalized autumn DMI is higher (lower) than one (minus one). Using this method, 10 positive IOD events are identified, including 1961, 1972, 1982, 1991, 1994, 1997, 2002, 2006, 2015 and 2019, and 8 negative IOD events are selected (1960, 1975, 1996, 1998, 2005, 2010, 2016 and 2021). More than half (54%) of the positive PMM years (1972, 1982, 1997, 2002, and 2015) are followed by positive IOD events in the following autumn, and many negative PMM years (1960, 1975, 1998 and 2021) are followed by negative IOD events in the following autumn. In particular, the super positive IOD events in the past (i.e. 1972 and 1997) were preceded by extreme positive PMM

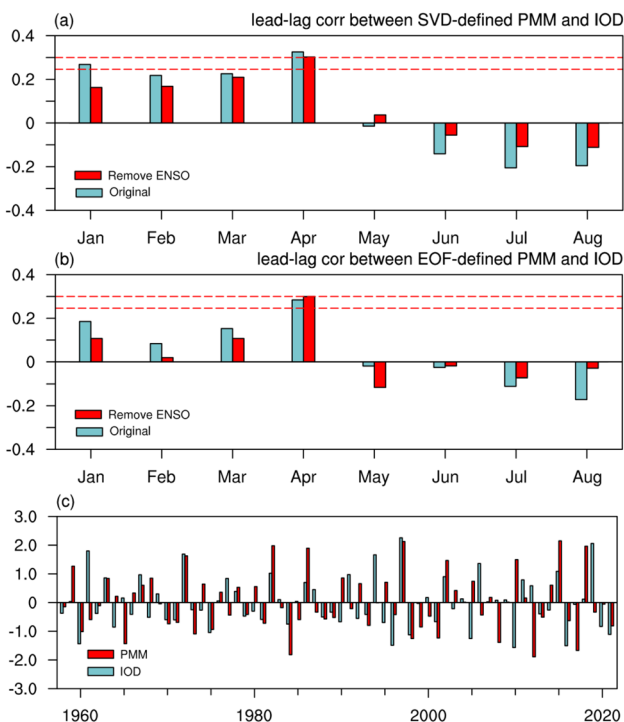
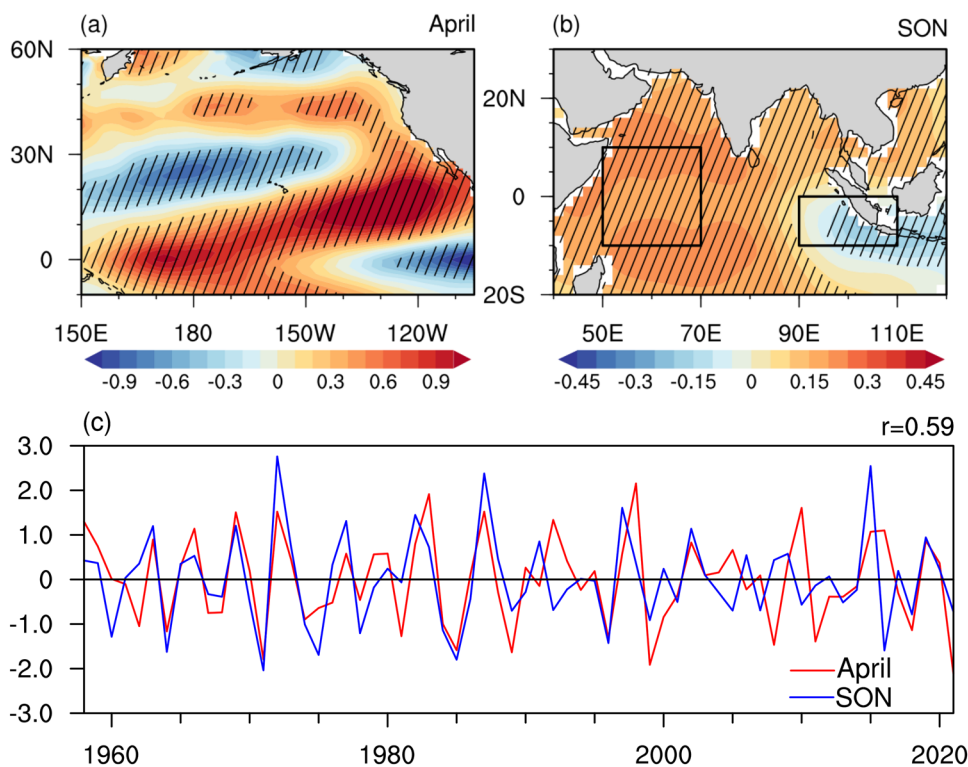


Fig. 1 a Lead-lag correlation coefficients between the autumn (September–October–November, SON) IOD index and the PMM index over the period 1958–2021 (blue bars). Two red horizontal lines denote the correlation significant at the 95% and 99% confidence levels, respectively. The red bar indicates preceding winter ENSO signal has been subtracted from the PMM index by means of linear regression. b As in (a), but for the EOF-defined PMM index. c Normalized time series of the spring PMM index and the following autumn IOD index

Fig. 2 The first SVD mode (SVD1) between interannual variations of spring (April) in the subtropical northeastern Pacific and the following autumn SST anomalies in the tropical Indian Ocean during 1958–2021. **a** Spring SST homogeneous regression map ($^{\circ}\text{C}$). **b** Autumn SST homogeneous regression map ($^{\circ}\text{C}$). **c** Normalized EC time series for spring and autumn SST of the SVD1. spring (autumn) SST homogeneous regression map is obtained by regressing the spring (autumn) SST anomalies onto the corresponding EC time series. Stippling in **(a)** and **(b)** indicates anomalies significant at the 95% confidence level



values. Thus, the spring PMM is a potential predictor for the IOD prediction in the following autumn.

We also employ the SVD technique to confirm the close linkage of the spring PMM with the following autumn IOD. The SVD technique could capture the co-varying pattern between two anomalous fields (Bretherton et al. 1992; Wallace et al. 1992; Cherry 1996; Von Storch and Zwiers 1999). Figure 2 shows the first SVD mode (SVD1) of spring SST anomalies in the subtropical northeast Pacific (21°S to 32°N and from 175° to 265°E) and following autumn SST anomalies in the tropical IO (15°S to 15°N and 50° to 110°E) over 1958–2021. The first SVD mode explains 76% of the total squared covariance. Spring SST anomalies in the Pacific associated with the SVD1 are featured by a prominent positive PMM-like pattern (Fig. 2a), with warm SST anomalies appearing off the west coast of North America and extending southwestward to the tropical central Pacific, together with cold SST anomalies in the tropical eastern Pacific and subtropical central North Pacific (Chiang and Vimont 2004; Chang et al. 2007; Amaya 2019). Autumn SST anomalies in the IO associated with the SVD1 are characterized by warm SST anomalies in the WTIO, and cold SST anomalies in the SETIO (Fig. 2b), forming a positive IOD-like pattern (Saji et al. 1999). The correlation coefficient between the two-expansion coefficient (EC) time series of the first SVD mode reaches 0.59, which is significant at

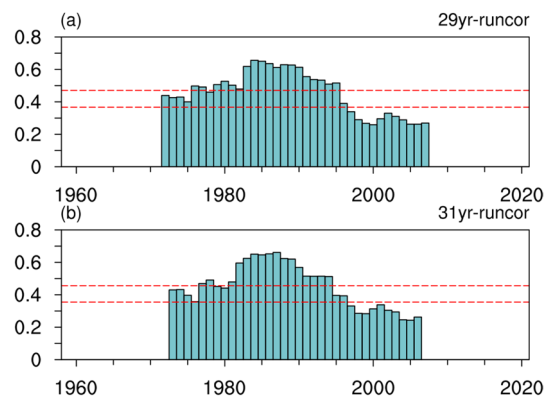


Fig. 3 Moving correlation between the spring PMM index and autumn IOD index with a running window of 29 **(a)** and 31 **(b)** years. The two red horizontal lines indicate the correlation coefficient that significant at the 95% and 99% confidence levels, respectively

the 99% confidence level according to the two-tailed Student's *t*-test. Therefore, the above evidence together suggest a close relationship between the spring PMM and autumn IOD.

We further examined the stability of the relationship by calculating moving correlation coefficients between the

spring PMM index and the autumn IOD index with different lengths of moving windows (Fig. 3). Different lengths of moving correlations all suggest a significant relationship between the spring PMM and the autumn IOD from 1958 to 2010 (Fig. 3). In contrast, the correlation between spring PMM and autumn IOD is weak after the 2010. This suggests that the connection between spring PMM and autumn IOD undergoes an interdecadal change around the 2010. In the following, the analysis period is focused on 1958–2010, over which the spring PMM-autumn PMM connection is significant.

4 Physical processes for the impact of PMM on IOD

4.1 Evolutions of SST, wind, and precipitation anomalies

In this section, the physical mechanism for the impact of the spring PMM on autumn IOD is examined. Figure 4 shows the evolution of SST, 850-hPa winds and precipitation anomalies from spring to autumn in association

with the spring PMM index over the period 1958–2010. Note that the spatial patterns of the spring PMM-related precipitation anomalies obtained from the NCEP-NCAR are highly similar to those derived from the CMAP and GPCP (Figures not shown). Hence, in the following, we only present the results obtained from the NCEP-NCAR. SST, wind and precipitation anomalies are weak in the IO in late-spring (April–May, AM for short) and early-summer (June–July, JJ for short; Fig. 4a, b, e, f, i, j). In the IO, clear SST, precipitation and wind anomalies occur in late-summer (August–September, AS for short) (Fig. 4c, d, g, h, k, l). In particular, significant southeasterly wind anomalies occur off the west coast of Sumatra Island, together with easterly wind anomalies over the equatorial IO in AS (Fig. 4g). The southeasterly wind anomalies off the west coast of Sumatra Island have been demonstrated to be a key trigger for the IOD occurrence (Saji et al. 1999; Li et al. 2003; Cai et al. 2013; Lee et al. 2022; Cheng et al. 2023). Specifically, the PMM-induced southeasterly wind anomalies off Sumatra, superimposed on the climatological southeasterly wind, would increase the total wind speed and contribute to SST cooling in the SETIO via enhancement of the upward latent heat flux

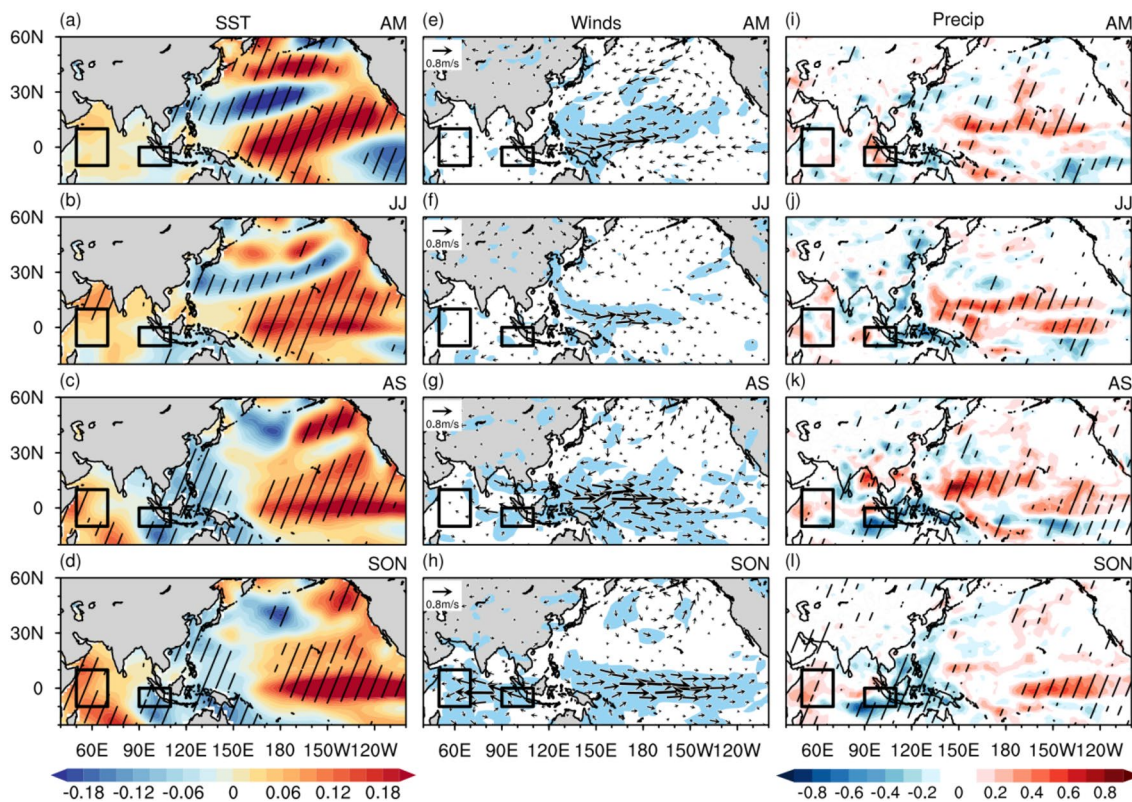


Fig. 4 Anomalies of SST (a–d, unit: °C), 850-hPa winds (e–h, unit: $m s^{-1}$) and precipitation (i–l, unit: $mm day^{-1}$) over Pacific region in AM (a, e, i), JJ (b, f, j), AS (c, g, k) and SON (d, h, l) regressed upon the normalized spring PMM. Shadings in e–h indicate either compo-

nent of the wind anomalies significant at the 95% confidence level. Slashed areas in a, b, c, d, i, j, k and l indicate anomalies significant at the 95% confidence level

(Fig. 4c; Xie and Philander 1994). In addition, in response to the PMM-associated anomalous southeasterly winds, the positive wind stress curl anomalies lead to upwelling Ekman pumping to enhance SST cooling in the SETIO (Fig. 4c). Correspondingly, the increased zonal SST gradient and anomalous easterly winds develop and intensify in the tropical IO via positive air-sea interaction in the following autumn (Fig. 4d, h), accompanied by marked positive (negative) precipitation anomalies over the WTIO (SETIO) (Fig. 4l). Finally, an IOD-like pattern is formed in autumn (Fig. 4d, h, l).

The PMM-related SST anomalies in AM in the Pacific show warm anomalies in the tropical central Pacific extending northeastward to the west coast of North America, accompanied by cold anomalies in the subtropical central North Pacific and tropical eastern Pacific (Fig. 4a). Positive precipitation anomalies are seen over the tropical central Pacific due to SST warming there (Fig. 4i). In addition, a significant cyclonic anomaly is established over the subtropical western North Pacific (Fig. 4e), together with northeasterly wind anomalies to its eastern side and southwesterly wind anomalies to its western side. The AM SST warming and enhanced atmospheric heating (indicated by positive precipitation anomalies) in the subtropical North Pacific (Figs. 4a, i) favour the occurrence of westerly wind anomalies over the equatorial western Pacific via a Gill type atmospheric response (Gill 1980; Hu et al. 2021; Chen et al. 2023; Fig. 4f). Subsequently, the SST warming, westerly wind and positive precipitation anomalies over the tropical Pacific maintain and develop to an El Niño event in the succeeding winter via positive air-sea feedback in the tropics (Fig. 4c, d, g, h, k, l).

Studies have pointed out that SST and atmospheric anomalies in the tropical Pacific could influence the occurrence and development of IOD (Annamalai et al. 2003;

Kajikawa et al. 2003; Huang and Shukla 2007; Du et al. 2013; Wang and Wang 2014; Zhang et al. 2018; Hu et al. 2021). In particular, the tropical Walker circulation plays an important role in linking the Pacific and Indian Oceans (Xie et al. 2002; Luo et al. 2010; Zhang et al. 2015; Tozuka et al. 2016; Ham et al. 2017). To confirm the role of the tropical Walker circulation in affecting the development of the IOD in association with the PMM, we examine the zonal–vertical circulation anomalies averaged in the tropics (Fig. 5). In AM, marked ascending anomalies appear over the tropical central Pacific, while descending anomalies are no apparent (Fig. 5a). In the following summer and autumn, a clear anomalous tropical Walker circulation is seen in the tropical Pacific, with pronounced ascending anomalies over the tropical central Pacific corresponding to warm SST and positive precipitation anomalies there (Fig. 5b, c), and descending anomalies over the Maritime continent and the tropical western Pacific (Fig. 5b, c). These descending anomalies over the Maritime continent contribute to the appearance of southeasterly wind anomalies off the west coast of Sumatra and Java (Cheng et al. 2023).

4.2 Roles of the surface heat fluxes and oceanic dynamics

The above analysis suggests that the SST and atmospheric anomalies over the subtropical North Pacific in association with the spring PMM propagate southward to tropical central and eastern Pacific via wind-evaporation-SST feedback process. Then, SST and associated precipitation anomalies over the tropical central and eastern Pacific induce southeasterly wind anomalies over the SETIO via modulation of the tropical Walker circulation. Finally, the SETIO southeasterly wind anomalies trigger the IOD event.

Fig. 5 Anomalies of equatorial zonal–vertical circulation in AM (a), JJ (b), AS (c), and SON (d) regressed upon the spring PMM index. Shadings indicate either component of the wind anomalies significant at the 95% confidence level

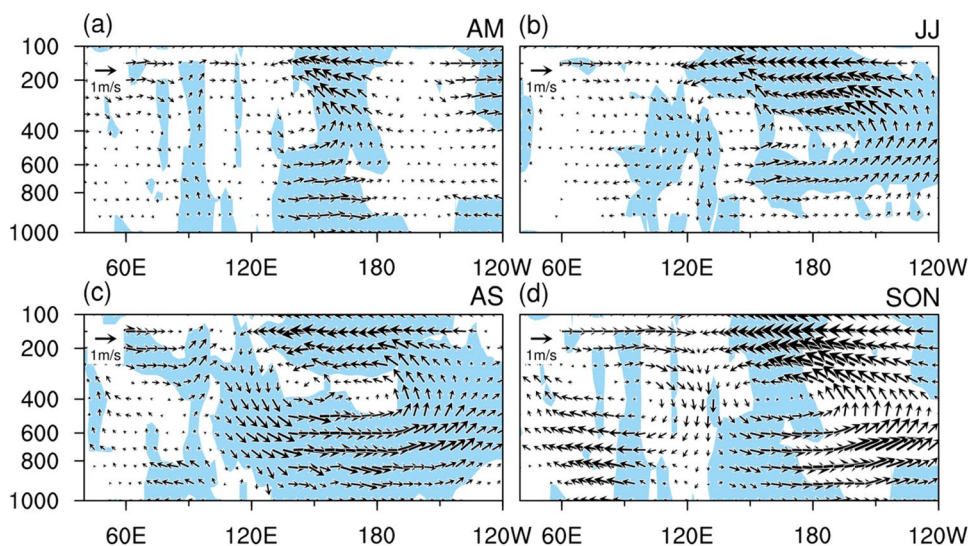
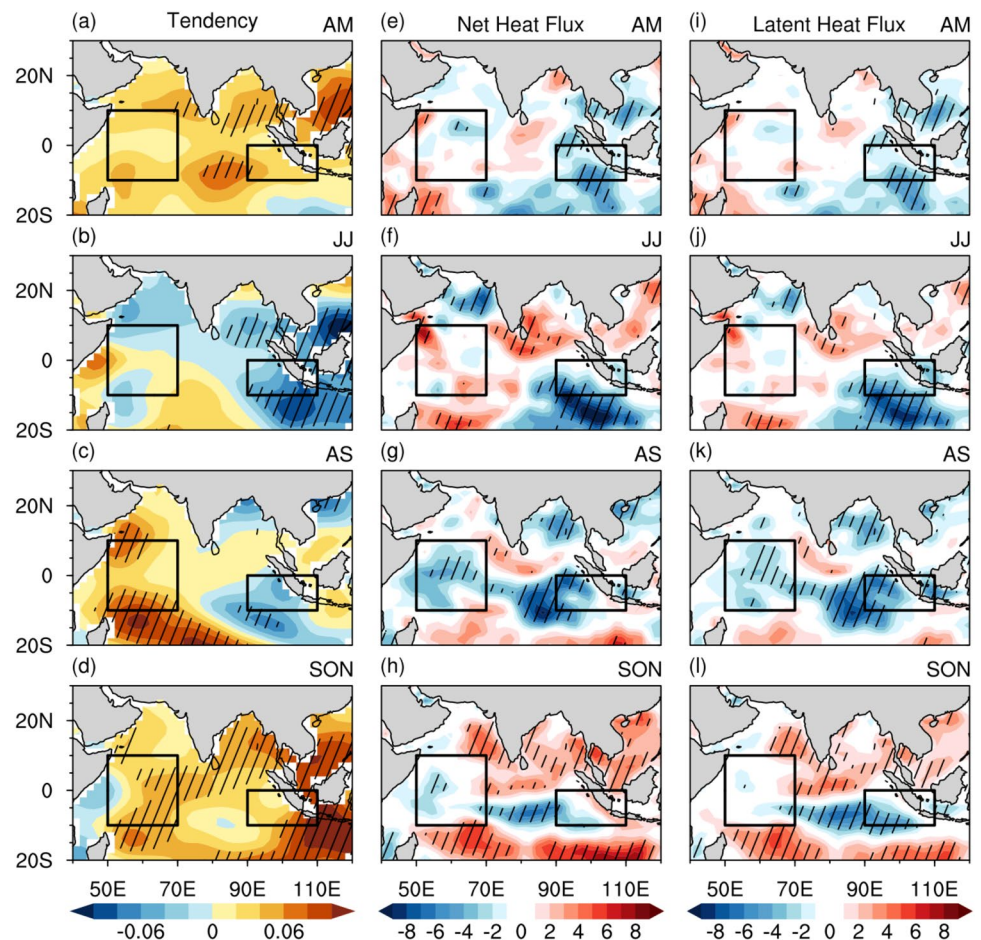


Fig. 6 Anomalies of SST tendency (**a–d**, unit: $^{\circ}\text{C}$), net surface heat flux (**e–h**, unit: Wm^{-2}) and latent heat flux (**i–l**, unit: Wm^{-2}) over the tropical Indian Ocean in AM (**a**, **e**, **i**), JJ (**b**, **f**, **j**), AS (**c**, **g**, **k**) and SON (**d**, **h**, **l**) regressed upon the normalized spring PMM. Slashed areas indicate anomalies significant at the 95% confidence level



In the following, we further examine how does the wind anomalies over the tropical IO generated by the spring PMM contribute to the formation of the IOD. We first examine the evolution of the SST tendency, net surface heat flux, and latent heat flux anomalies associated with the spring PMM in Fig. 6. Here, we use the central difference method to define the SST tendency. For example, the SST tendency in May is calculated as the difference of the SST anomalies in June minus that in April divided by two. Net surface and latent heat fluxes that warm the SST are defined as positive signs and those that cool the SST are defined as negative. We focus on the two key regions of the IOD, including the WTIO and the SETIO. The SETIO is featured by significant negative SST tendency anomalies in JJ (Fig. 6b), while in AS and autumn, the anomalous negative SST tendency gradually weakens (Fig. 6c, d). As for the WTIO, pronounced positive SST tendency anomalies dominate in the AS and persist until the autumn (Fig. 6c, d).

The anomalous southeasterly winds over the SETIO in JJ and AS (Fig. 4f, g) lead to an increase in the surface wind speed and contribute to the enhancement of the upward surface latent heat flux and SST cooling there (Fig. 6f, g, j,

k) (Cayan 1992). However, in the WTIO, as a result of the strengthened easterly wind anomalies over the tropical IO (Fig. 4g), negative surface latent heat flux anomalies dominate the WTIO in AS (Fig. 6g, k), suggesting that the surface heat flux anomalies contribute negatively to the formation of the warm SST anomalies in the western pole of the IOD. When the IOD peaks in autumn, the net surface heat flux anomalies over the WTIO and SETIO are also inconsistent with the SST tendency (Fig. 4d, h, l). The above analysis indicates that the formation of the SST tendency in the IOD development cannot be fully explained by the surface heat flux anomalies. Thus, the oceanic dynamical process also play a crucial role.

Longitude-depth cross-sections of potential temperature anomalies averaged over 10°S – 10°N are shown in Fig. 7. In AM and JJ, subsurface temperature anomalies are weak in tropical IO (Fig. 7a, b). In AS, significant subsurface cooling anomalies are seen in the SETIO, which maintain and develop into the following autumn (Fig. 7c, d). Clear subsurface warming anomalies begin to develop over the WTIO in AS (Fig. 7c) and increase significantly in the following autumn when the IOD reaches its peak phase. In general, the evolution of the subsurface temperature anomalies in the tropical IO (Fig. 7) corresponds well to the SST anomalies

Fig. 7 As in Fig. 5, but for vertical potential temperature (unit: °C) anomalies calculated as the average over 10° S–10° N. Black curves indicate the climatological thermocline depth

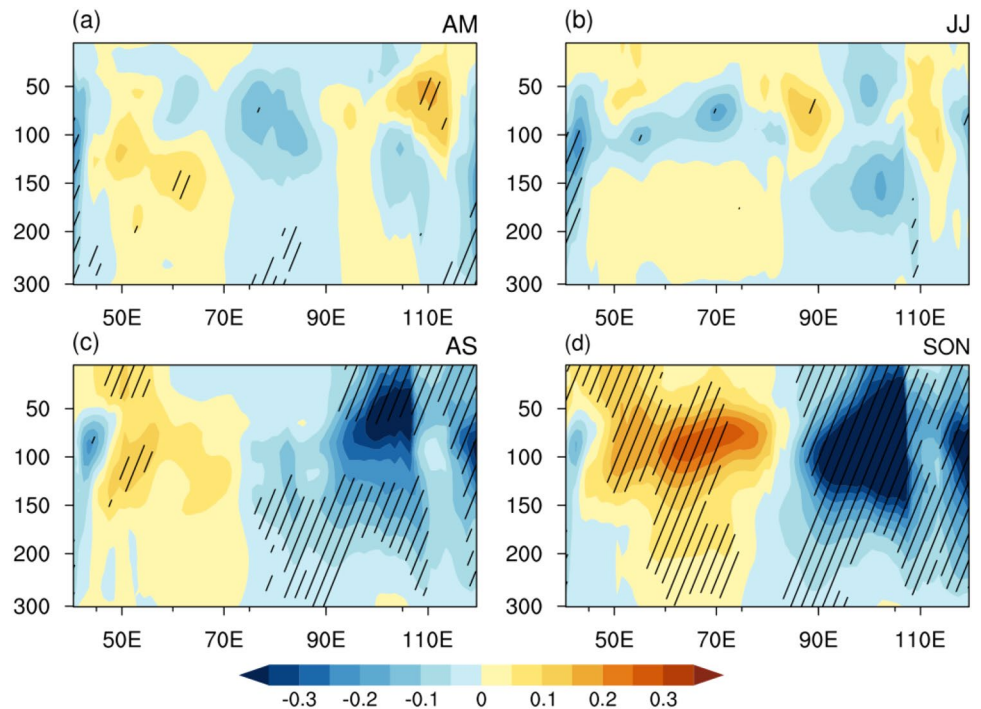


(Fig. 4a–d). Therefore, the ocean dynamical process is also essential for the evolution of IOD-like SST anomalies in the tropical IO associated with the spring PMM.

4.3 Ocean mixed layer heat budget

To examine the relative contribution of the air–sea interaction and ocean dynamical process to the development of IOD-like SST anomalies, the ocean mixed-layer heat budget is diagnosed (Fig. 8). In particular, we calculate the contributions on each term in Eq. (3). Note that the SST tendency is not exactly equal to the sum of the zonal, meridional, entrainment, and the net surface heat flux due to the coarse temporal and spatial resolution of the datasets, different data sources for ocean and heat flux, and uncertainties in parameterisation (Huang et al. 2010; Cheng et al. 2023). In the WTIO, the positive SST tendency starts to develop in AS and enhances in autumn (Fig. 8a), supporting the formation of positive SST anomalies there (Fig. 4c, d). Positive SST anomalies in the WTIO are mainly due to the positive zonal ocean advection and entrainment since the AS (Fig. 8a). In the SETIO, the appearance of the large negative SST tendency in JJ and AS is due to the combined effect of the net surface heat flux and entrainment (Fig. 8b). Thus, both the surface heat flux change and the oceanic process contribute to the development of the SST anomalies in the IO associated with the spring PMM.

Next, we examine which components of the surface heat flux and ocean dynamic play a dominant role according to Eq. (6). In the WTIO, the key ocean dynamical processes

for the subsurface warming in the AS and autumn are the entrainment term and the zonal ocean advection term (Fig. 8a). Furthermore, the entrainment in the WTIO is mainly determined by the thermocline feedback term (i.e., $\overline{w_e' \frac{T_a' - T_h'}{h}}$) and the Ekman feedback term (i.e., $w_e' \frac{T_a' - T_h'}{h}$) (Fig. 8c). As mentioned above, the anomalous easterly winds over the tropical IO in AS (Fig. 4g) could induce an oceanic Rossby wave, which can quickly propagate to the WTIO, resulting in anomalous downwelling ($w_e' < 0$) and subsurface warming there ($\frac{T_a' - T_h'}{h} < 0$). Considering that climatological oceanic upwelling ($\overline{w_e} > 0$) is dominant in the WTIO, therefore, both the thermocline and Ekman feedbacks contribute positively to the subsurface warming in the WTIO. Meanwhile, our results also indicate that the mean current effect ($\overline{u_a} \frac{\partial T_a'}{\partial x}$) is the key term of the zonal ocean advection that supports subsurface warming in the WTIO (Fig. 8e). As for the SETIO, net heat flux and entrainment contribute largely to the subsurface cooling in JJ and AS (Fig. 8b). The thermocline feedback (i.e., $\overline{w_e' \frac{T_a' - T_h'}{h}}$) dominates the entrainment term in the SETIO (Fig. 8d). In particular, southeasterly wind anomalies in AS over the SETIO (Fig. 4g) could induce anomalous upwelling of the cold water and lead to subsurface cooling ($\frac{T_a' - T_h'}{h} < 0$). Due to the climatological ocean downwelling ($\overline{w_e} < 0$) in the SETIO, the thermocline feedback ($\overline{w_e' \frac{T_a' - T_h'}{h}}$) contributes to the subsurface cooling there. In addition, the net surface heat flux is mainly dominated by the surface latent heat flux anomalies over the SETIO (Fig. 8f). In brief summary, atmospheric circulation anomalies over the tropical IO induced by the spring PMM contribute to the occurrence and development of IOD-like

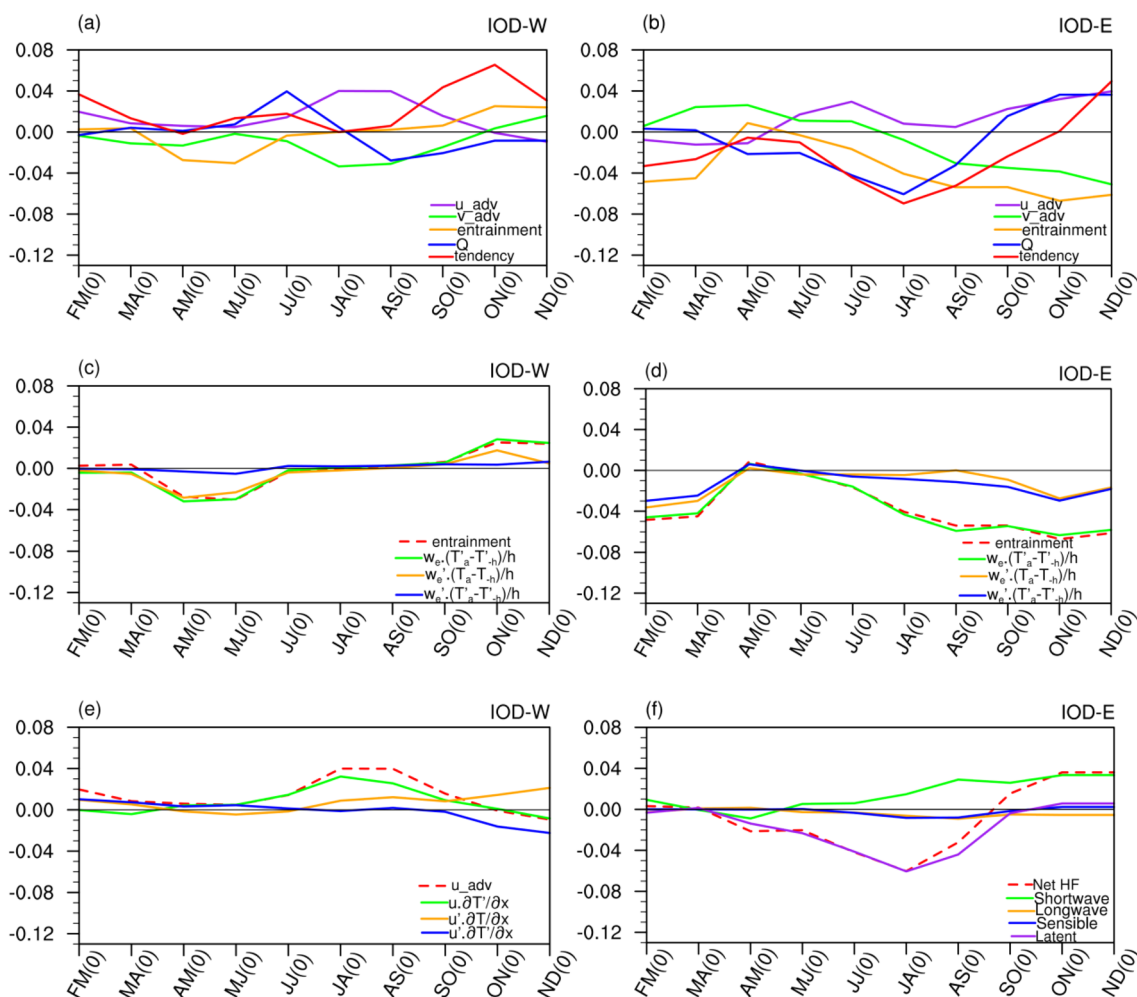


Fig. 8 Bimonthly averaged anomalies of total zonal advection (purple line), meridional advection (green line), entrainment (orange line), surface net heat flux (blue line), and temperature tendency (red line) over **a** the western Indian Ocean (50°–70° E, 10° S–10° N) and **b** the eastern Indian Ocean (90°–110° E, 10° S–0°) regressed onto the normalized spring PMM index. Bimonthly averaged anomalies of entrainment (red dashed line), the anomalous vertical advection by the anomalous temperature and mean current (green line), the anomalous vertical advection by the mean temperature and anomalous current (orange line), and the non-linear vertical advection by

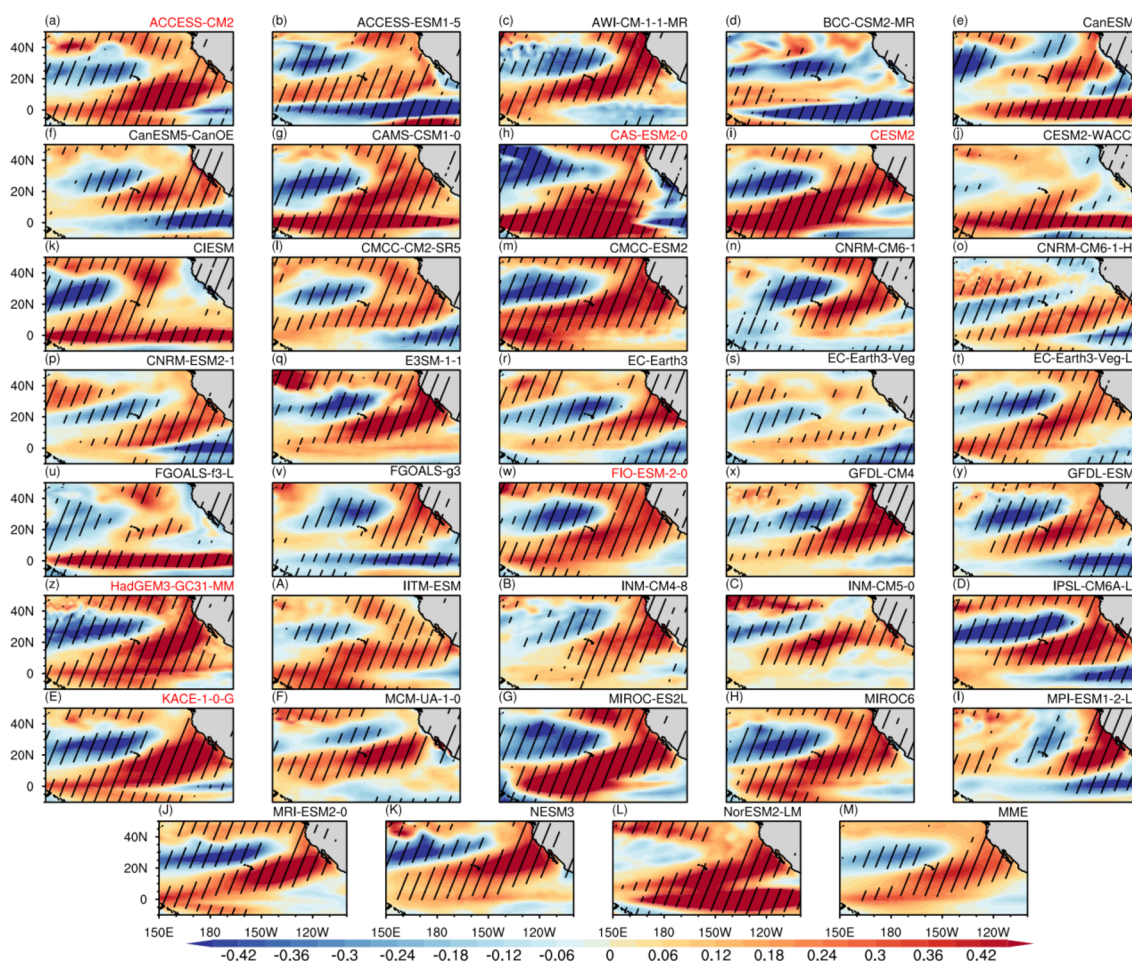
the anomalous temperature and current (blue line) over **c** the western Indian Ocean (50°–70° E, 10° S–10° N) and **d** the eastern Indian Ocean (90°–110° E, 10° S–0°) regressed onto the normalized spring PMM index. **e** is as in **(c)**, but for zonal advection. Bimonthly averaged anomalies of net surface heat flux (purple line), surface short-wave radiation (green line), surface long-wave radiation (orange line), surface sensible heat flux (blue line), and surface latent heat flux (red line) over **f** the eastern Indian Ocean (90°–110° E, 10° S–0°) regressed onto the normalized spring PMM index

SST anomalies both via modulating the surface heat flux and the oceanic dynamics.

4.4 Linkage of spring PMM with autumn IOD in climate model simulation

In the following, we examine the ability of 38 coupled climate models participated in CMIP6 in capturing the linkage between the spring PMM and the following autumn IOD. Figure 9a–L shows spatial pattern of spring PMM represented by spring SST anomalies in North Pacific regressed upon the spring PMM index. Figure 9N displays spatial

correlations of the PMM-related SST anomalies in the North Pacific between the 38 CMIP6 models and observations. It shows that many CMIP6 models can well simulate the spatial patterns of PMM with warm SST anomalies off the west coast of North America extending southwestward to the tropical central Pacific, together with cold SST anomalies in the tropical eastern Pacific and subtropical central North Pacific. However, there are also several models with poor simulation of PMM (such as ACCESS-ESM1-5, BCC-CSM2-MR, CanESM5, CESM2-WACCM, CIesm, FGOALS-f3-L, FGOALS-g3 and NorESM2-LM), with pattern correlation less than 0.55. We have also examined the



(N) PMM Pattern Correlation

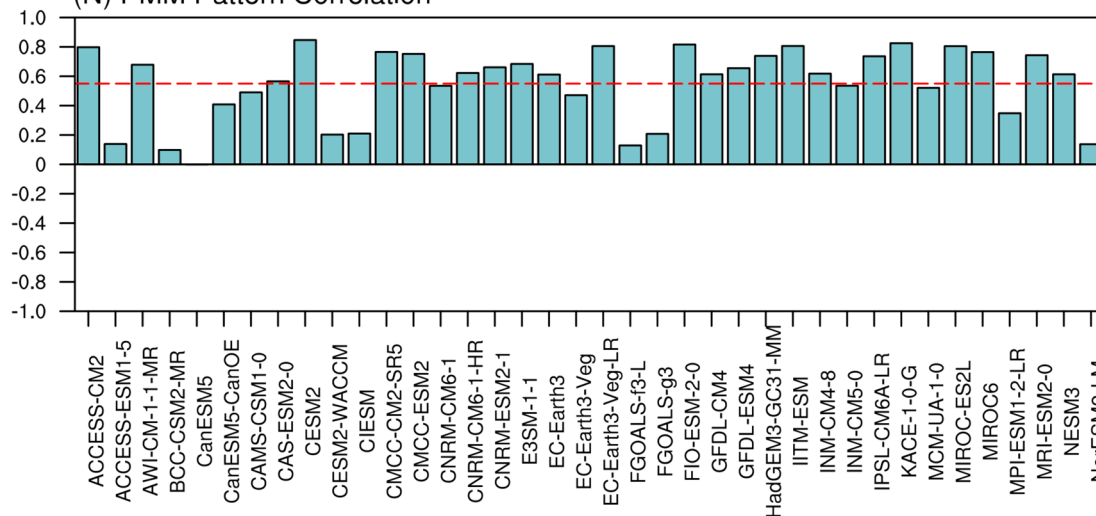


Fig. 9 a–L Regression maps of SST anomalies in MAM onto the normalized spring PMM index during 1958–2010 in 38 CMIP6 models. **M** The ensemble mean of the 38 CMIP6 models. The model ID is shown at the top right corner of each panel. The models marked with red ID are selected for composition in Figs. 12 and 13. Slashed areas

indicate anomalies significant at the 95% confidence level. **N** The spatial correlation coefficients of the PMM-related SST anomalies in the North Pacific between the 38 CMIP6 models and observations. The red horizontal line denotes the correlation coefficient of 0.55

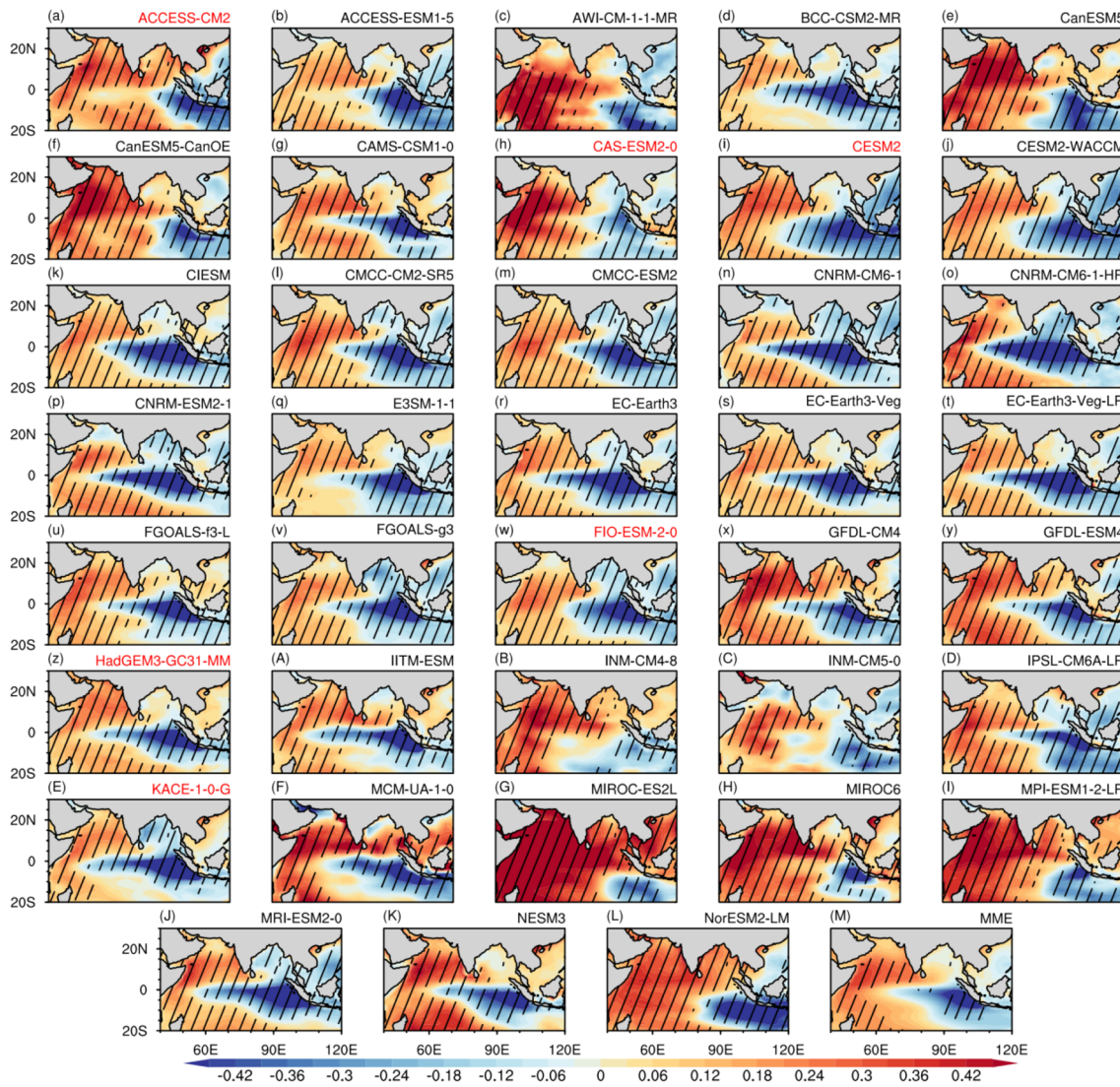
performance of the CMIP6 models in capturing the IOD. Spatial pattern of autumn IOD is represented by autumn SST anomalies in the tropical Indian Ocean regressed upon the autumn IOD index (Fig. 10a–L). Figure 10N calculates the spatial correlations of the IOD-related SST anomalies in the tropical Indian Ocean between the 38 CMIP6 models and the observations. The results indicate that most models could simulate the IOD well, with warm (cold) SST anomalies in the tropical western (southeastern) Indian Ocean. However, the positive IOD-related cold SST anomalies in the tropical eastern Indian Ocean are too strong and extend much westward in many models (such as CNRM-CM6-1, CNRM-ESM2-1, EC-Earth3-Veg-LR), consistent with previous studies showing that climate models tend to overestimate the amplitude of IOD (Cai et al. 2013). Previous studies have indicated that the stronger and westward-extending IOD-related cold SST anomalies in the tropical eastern Indian may be due to the stronger thermocline-SST feedback in the tropical eastern Indian Ocean in climate models (Cai and Cowan 2013). Based on the above analysis, there are a total of 23 models that simulate PMM well (with pattern correlation more than 0.55), 33 models that simulate IOD well (with pattern correlation more than 0.65), and 20 models that simulate both PMM and IOD well. Thus, we finally select 20 models that have a good performance in capturing the PMM and IOD to examine the linkage between the spring PMM and the autumn IOD. Figure 11 shows the correlation coefficient between the spring PMM index and the autumn IOD index in these 20 models. From Fig. 11, six models (i.e. ACCESS-CM2, CAS-ESM2-0, CESM2, FIO-ESM-2-0, HadGEM3-GC31-MM, KACE-1-0-G) could capture the close connection of the spring PMM with the following autumn IOD. In the following, we further examine the physical process for the impact of the spring PMM on the following autumn IOD based on these six selected models.

Figure 12 shows the evolution of the SST, 850-hPa winds, and precipitation anomalies associated with the PMM for the ensemble mean of the 6 selected models. Most of the processes obtained from the models are similar to those in the observations. As mentioned above, there are three key processes linking the spring PMM and the autumn IOD. First, the SST, precipitation and atmospheric circulation anomalies associated with the PMM could be maintained over the subtropical North Pacific and extended to the tropical central Pacific in the following summer via the WES feedback. Second, the spring PMM-induced summer SST and precipitation anomalies in the tropical central-eastern Pacific lead to atmospheric circulation anomalies over the tropical IO via modulation of the tropical Walker circulation. Third, the spring PMM-induced atmospheric circulation anomalies in the tropical IO further lead to the occurrence and development of IOD-like SST anomalies. In general, the 6 models can well capture the above processes well in relaying the

impact of the spring PMM on the following autumn IOD. In particular, a PMM pattern could be seen in spring, with marked warm SST and westerly wind anomalies over the central-western Pacific (Fig. 12a, e). In the following summer and autumn, the anomalous SST, winds, and precipitation extend to the tropical central-eastern Pacific (Fig. 12b, c, f, g, j, k). Furthermore, an anomalous tropical Walker circulation is seen with an ascending branch over the tropical eastern Pacific and a descending branch and suppressed atmospheric heating anomalies over the Maritime Continent in summer and autumn (Figs. 12j, k, 13b, c). Then, southeasterly wind anomalies caused by the anomalous Walker circulation lead to cold SST anomalies in the SETIO, which further contribute to the appearance and development of a IOD-like SST anomaly pattern (Fig. 12c, g). In summary, the main mechanisms for the influence of spring PMM on the following autumn IOD can be validated in the long simulation of coupled climate models.

5 Conclusion and discussion

This study demonstrated that the spring PMM has a significant relationship with the following autumn IOD, which is independent of the preceding winter ENSO. The physical process for the impact of the spring PMM on the autumn IOD is shown schematically in Fig. 14. First, a positive spring PMM is associated with a tripole SST pattern and a significant cyclonic circulation over the North Pacific. The SST and atmospheric anomalies associated with the PMM over the North Pacific extend to the tropical Pacific in the following summer via the WES feedback. SST warming in the tropical central-eastern Pacific leads to positive precipitation and enhanced atmospheric heating there. Then, an anomalous tropical Walker circulation is induced, with ascending anomalies in the tropical central-eastern Pacific and descending anomalies in the tropical western Pacific and the Maritime Continent (Fig. 14). Moreover, the descending motion and associated suppressed atmospheric heating anomalies around the Maritime Continent lead to the occurrence of southeasterly wind anomalies off the west coast of the Sumatra. These anomalous southeasterly winds contribute to SST cooling in the SETIO by strengthening the upwelling of cold water and enhancement of upward surface net surface heat flux. The appearance of cold SST anomalies in the SETIO then contributes to the increased zonal gradient of SST anomalies in the equatorial IO, and result in easterly wind anomalies over the equatorial IO in summer. These easterly wind anomalies lead to SST warming in the WTIO via modulation of oceanic zonal and vertical heat transport. The process for the spring PMM-autumn IOD linkage can also be found in the long historical simulation of coupling models. In addition to the PMM, other extratropical climate



(N) IOD Pattern Correlation

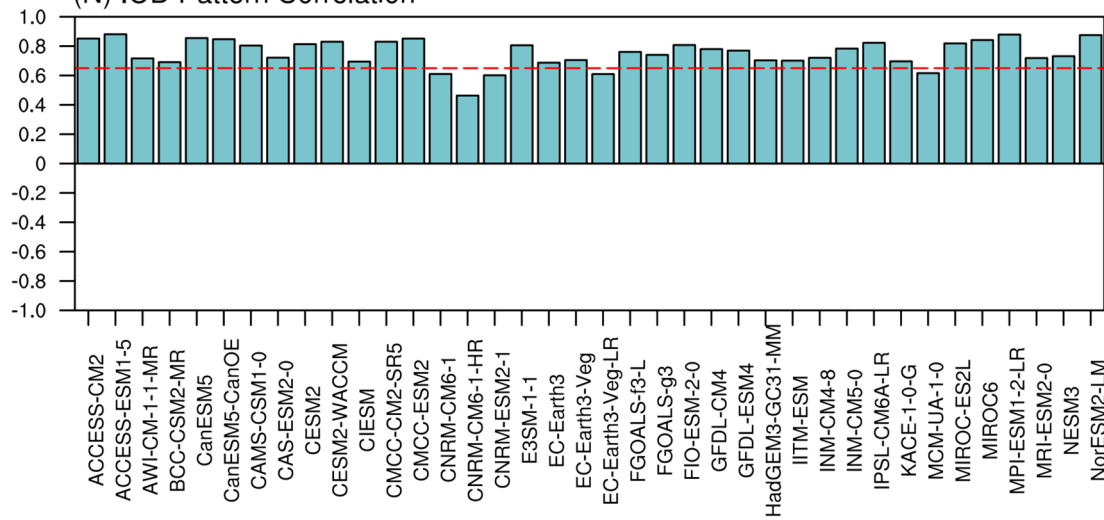


Fig. 10 a–L Regression maps of SST anomalies in SON onto the normalized autumn IOD index during 1958–2010 in 38 CMIP6 models. **M** The ensemble mean of the 38 CMIP6 models. The model ID is shown at the top right corner of each panel. The models marked with red ID are selected for composition in Figs. 12 and 13. Slashed areas indicate anomalies significant at the 95% confidence level. **N** The spatial correlation coefficients between IOD-related SST anomalies in the tropical Indian Ocean between the 38 CMIP6 models and the observations. The red horizontal line denotes the correlation coefficient of 0.65

variability (such as the North Pacific Oscillation and the Victoria mode) could also have a significant impact on the tropical Pacific SST (Ding et al. 2017, 2022; Vimont et al. 2003). We will further explore the combined influences of these extratropical climate variability on the IOD in the near future.

Our study indicated that the relationship between the spring PMM and the autumn IOD has experienced a significant interdecadal change around the early-2000s. Then, a question is: what is the possible factors leading to this interdecadal change. To address this issue, we have examined

the evolution of SST, 850-hPa winds and precipitation anomalies in association with the spring PMM index during 1958–2010 (high correlation period) and 2010–2021 (low correlation period) (Figures not shown). Significant warm SST anomalies associated with the spring PMM appear in the tropical central Pacific in AM and JJ during 1958–2010. These tropical central Pacific SST anomalies then can effectively influence the tropical walker circulation, which further exert an impact on the IOD development. By contrast, SST and precipitation anomalies in the tropical Pacific in AM and JJ are weak during 2010–2021. As such, the related anomalous tropical Walker circulation induced by the spring PMM is much weaker and less significant during 2010–2021. Thus, the impact of the spring PMM on the following IOD is weak during 2010–2021. Above analysis indicates that change in the relationship between the spring PMM and autumn IOD may be due to change in the strength and location of the SST and atmospheric heating anomalies in the tropical Pacific caused by the spring PMM. Further work is needed to investigate the reasons for the above differences caused by the spring PMM.

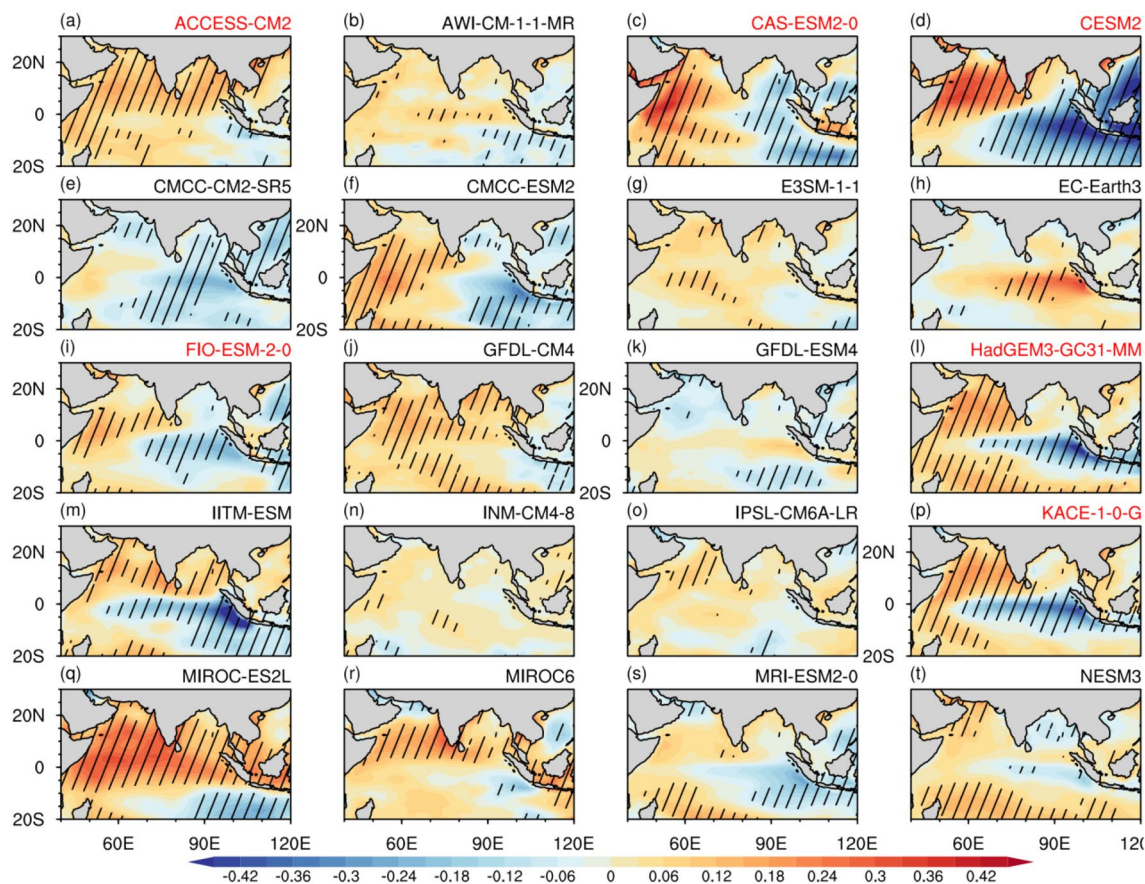


Fig. 11 a–t Regression maps of SST anomalies in SON onto the normalized spring PMM index during 1958–2010 in 38 CMIP6 models. The model ID is shown at the top right corner of each panel. The

models marked with red ID are selected for composition in Figs. 12 and 13. Slashed areas indicate anomalies significant at the 95% confidence level

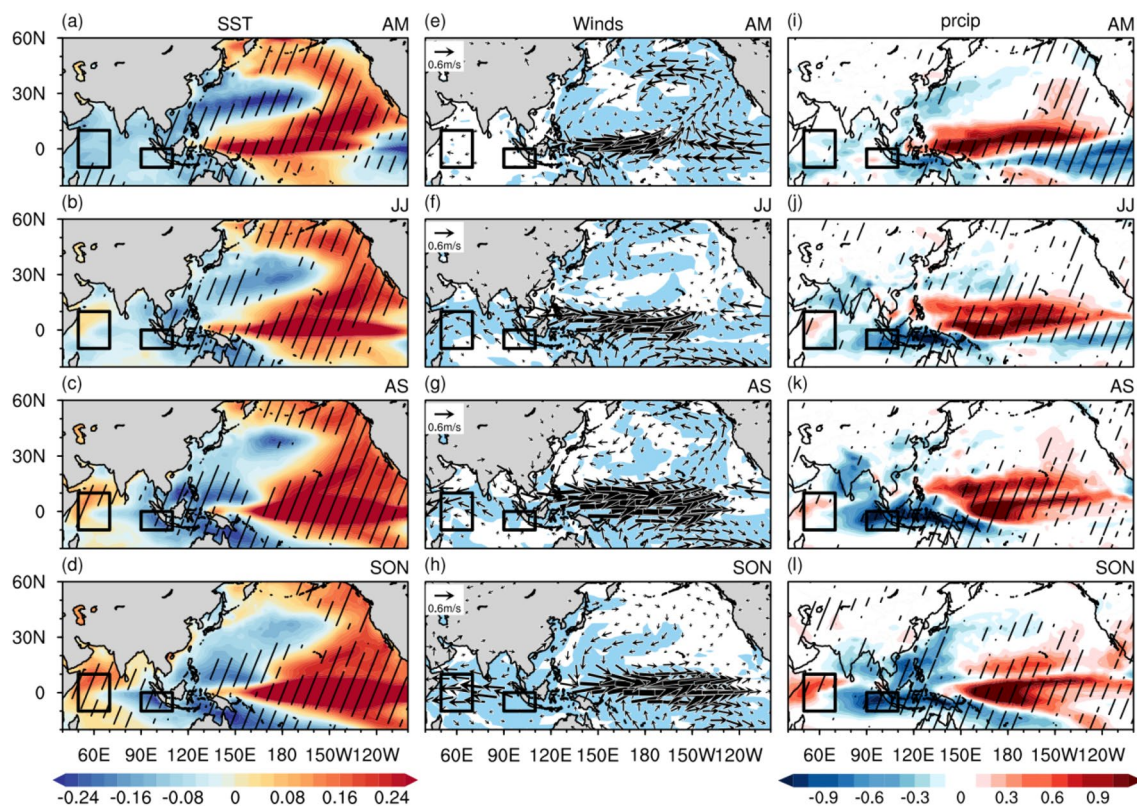
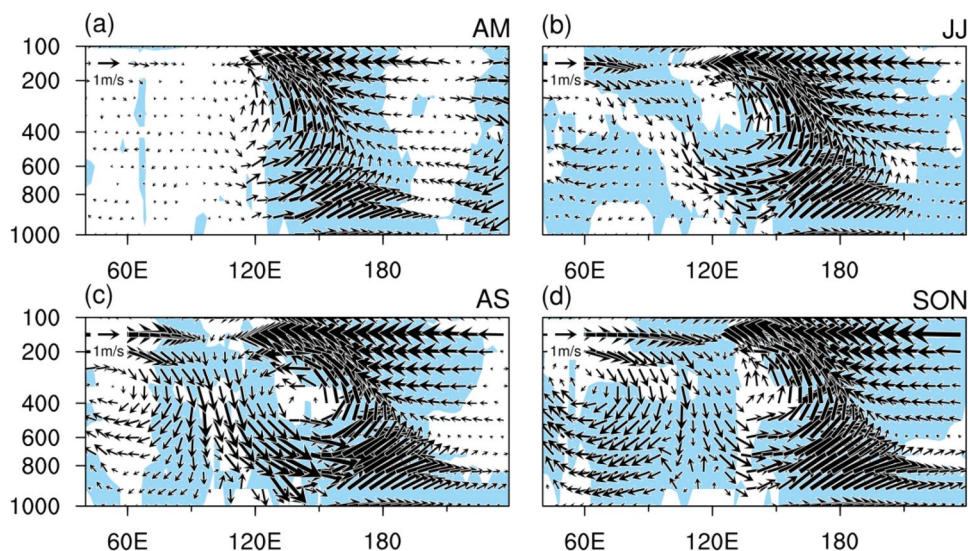


Fig. 12 As in Fig. 4, but for the simulation for the ensemble mean of the 6 selected CMIP6 models during 1958–2010

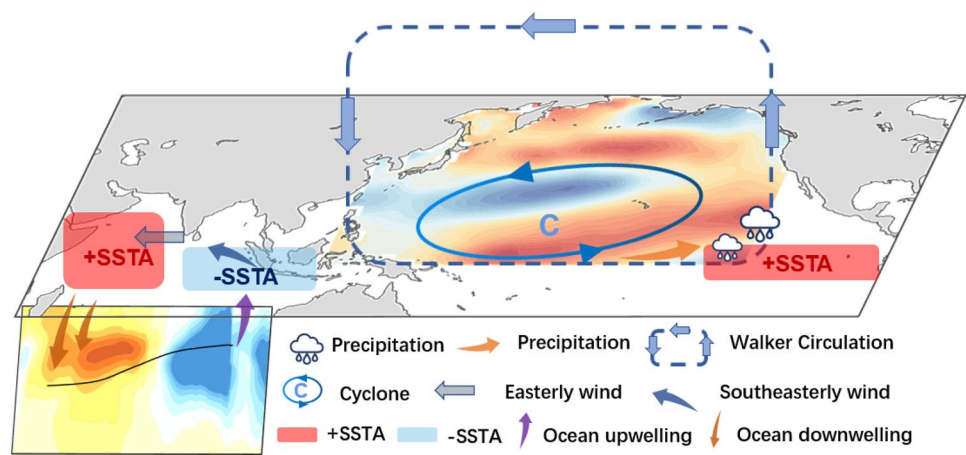
Fig. 13 As in Fig. 5, but for the simulation for the ensemble mean of the 6 selected CMIP6 models during 1958–2010



In addition to the canonical IOD event (i.e. matures in autumn), there is another type of IOD event that tends to mature in summer (Jiang et al. 2022; Tao et al. 2023). We have calculated the lead-lag correlation coefficients between the early IOD index (defined by the summer DMI) and the PMM index over the period 1958–2021 (Figure not shown). Our preliminary results indicate that the correlation

coefficients between the early IOD index and the PMM indices in preceding months are relatively weak and statistically insignificant (Figure not shown). This implies that the PMM may have a weak impact on the development of the early IOD. Tao et al. (2023) suggested that the development of the early IOD event is mainly caused by the local ocean–atmosphere interaction within the tropical Indian Ocean.

Fig. 14 Schematic diagrams of physical processes of how the spring PMM influences the autumn IOD. The shading over the Pacific indicates the regression of SST anomalies (unit: °C) against the spring PMM index in AM. The longitude–depth cross-section over the Indian Ocean is the regression of potential temperature anomalies (unit: °C) against the spring PMM index in SON. Black curve in subsurface indicate the deepened (shallowed) thermocline in the western (eastern) Indian Ocean



This study found that only a subset of CMIP6 models were able to simulate the influence of spring PMM on the autumn IOD. Further analysis is needed to understand why other models were unable to capture the spring PMM–autumn IOD relationship. Furthermore, this study examined the impact of preceding PMM on the following autumn IOD. One may wonder whether the autumn IOD could have a feedback effect on the PMM. To address this issue, we have calculated the correlation coefficients between the summer and autumn IOD index with the PMM index in the following months. It shows that significant negative correlations are found between the JJ IOD index and the PMM index starting from September (Figure not shown). In addition, the AS IOD index shows a significant negative correlation with the PMM index starting from November (Figure not shown). These suggest that the preceding IOD indeed may have a feedback effect on the development of PMM with a lead time of two to three months. The physical process for the impact of the IOD on the following PMM remains to be explored.

Acknowledgements We thank two anonymous reviewers for their constructive suggestions, which helped to significantly improve the paper.

Author contributions SFC and WC designed the research, XC performed the analysis, XC and SFC wrote the manuscript. ZCD and XQL downloaded the CMIP6 data. All authors commented and revised the manuscript.

Funding This study was supported jointly by the National Natural Science Foundation of China (42175039 and 42205021).

Availability of data and material The NCEP/NCAR reanalysis data are obtained from <https://psl.noaa.gov/data/reanalysis/reanalysis.shtml>. SST data are obtained from <https://www.esrl.noaa.gov/psd/data/gridded/>. The GPCP precipitation data are derived from <https://psl.noaa.gov/data/gridded/data.gpcp.html>. The CMAP precipitation data are derived from https://www.cpc.ncep.noaa.gov/products/global_precip/html/wpage.cmap.html. Oceanic variables from GODAS are obtained from <http://www.cpc.ncep.noaa.gov/products/GODAS>. The historical simulation data of CMIP6 are obtained from <https://esgf-node.llnl.gov/search/cmip6/>.

Code availability (software application or custom code) All codes used in this study are available from the corresponding author.

Declarations

Conflict of interest The authors declare no potential conflicts of interest.

Ethics approval and consent to participate: Not applicable.

Consent for publication Not applicable.

References

- Adler RF et al (2003) The Version-2 Global Precipitation Climatology Project (GPCP) monthly precipitation analysis (1979–present). *J Hydrometeorol* 4:1147–1167
- Alexander MA et al (2002) The atmospheric bridge: the influence of ENSO teleconnections on air–sea interaction over the Global Oceans. *J Clim* 15:2205–2231. [https://doi.org/10.1175/1520-0442\(2002\)015](https://doi.org/10.1175/1520-0442(2002)015)
- Amaya DJ (2019) The Pacific meridional mode and ENSO: a review. *Curr Climate Change Rep* 5:296–307
- Anderson BT, Karspeck A (2013) Triggering of El Niño onset through trade wind-induced charging of the equatorial Pacific. *Geophys Res Lett* 40:1212–1216. <https://doi.org/10.1002/grl.50200>
- Anderson BT, Perez RC (2015) ENSO and non-ENSO induced charging and discharging of the equatorial Pacific. *Clim Dyn* 45:2309–2327. <https://doi.org/10.1007/s00382-015-2472-x>
- Annamalai H et al (2003) Coupled dynamics over the Indian Ocean: spring initiation of the Zonal Mode. *Deep Sea Res Part II* 50:2305–2330
- Aparna AR, Girishkumar MS (2022) Mixed layer heat budget in the eastern equatorial Indian Ocean during the two consecutive positive Indian Ocean dipole events in 2018 and 2019. *Clim Dyn* 58:3297–3315. <https://doi.org/10.1007/s00382-021-06099-8>
- Ashok K, Guan Z, Yamagata T (2001) Impact of the Indian Ocean Dipole on the relationship between the Indian monsoon rainfall and ENSO. *Geophys Res Lett* 28:4499–4502

- Ashok K, Behera SK, Rao SA, Weng H, Yamagata T (2007) El Niño Modoki and its possible teleconnection. *J Geophys Res* 112:C11007. <https://doi.org/10.1029/2006JC003798>
- Behera SK, Krishnan R, Yamagata T (1999) Unusual ocean-atmosphere conditions in the tropical Indian Ocean during 1994. *Geophys Res Lett* 26:3001–3004. <https://doi.org/10.1029/1999GL010434>
- Behera SK et al (2006) A CGCM study on the interaction between IOD and ENSO. *J Clim* 19:1688–1705. <https://doi.org/10.1175/jcli3797.1>
- Behringer D, Xue Y (2004) Evaluation of the global ocean data assimilation system at NCEP: the Pacific Ocean
- Bretherton CS, Smith C, Wallace JM (1992) An intercomparison of methods for finding coupled patterns in climate data. *J Clim* 5:541–560. [https://doi.org/10.1175/1520-0442\(1992\)005<0541:AIOMFF.2.0.CO;2](https://doi.org/10.1175/1520-0442(1992)005<0541:AIOMFF.2.0.CO;2)
- Bretherton CS, Widmann M, Dymnikov VP, Wallace JM, Bladé I (1999) The effective number of spatial degrees of freedom of a time-varying field. *J Clim* 12:1990–2009. [https://doi.org/10.1175/1520-0442\(1999\)012](https://doi.org/10.1175/1520-0442(1999)012)
- Cai WJ, Cowan T (2013) Why is the amplitude of the Indian Ocean Dipole overly large in CMIP3 and CMIP5 climate models? *Geophys Res Lett* 40:1200–1205
- Cai W, Van Rensch P, Cowan T, Hendon HH (2011) Teleconnection pathways of ENSO and the IOD and the mechanisms for impacts on Australian rainfall. *J Clim* 24:3910–3923
- Cai WJ, Zheng XT, Weller E et al (2013) Projected response of the Indian Ocean Dipole to greenhouse warming. *Nat Geosci* 6:999007. <https://doi.org/10.1038/ngeo2009>
- Cayan DR (1992) Latent and sensible heat flux anomalies over the Northern Oceans: the connection to monthly atmospheric circulation. *J Clim* 5:354–369. [https://doi.org/10.1175/1520-0442\(1992\)005](https://doi.org/10.1175/1520-0442(1992)005)
- Chang P, Zhang L, Saravanan R, Vimont DJ, Chiang JCH, Ji L, Seidel H, Tippett MK (2007) Pacific meridional mode and El Niño–Southern Oscillation. *Geophys Res Lett* 34:L16608. <https://doi.org/10.1029/2007GL030302>
- Chen SF, Yu B, Chen W (2014) An analysis on the physical process of the influence of AO on ENSO. *Clim Dyn* 42:973–989. <https://doi.org/10.1007/s00382-012-1654-z>
- Chen JP, Wang X, Zhou W, Wang CZ, Xie Q, Li G, Chen S (2018) Unusual rainfall in southern China in decaying august during extreme El Niño 2015/16: role of the Western Indian Ocean and North Tropical Atlantic SST. *J Clim* 31(17):7019–7034. <https://doi.org/10.1175/JCLI-D-17-0827.1>
- Chen SF, Chen W, Yu B, Wu R, Graf HF, Chen L (2023) Enhanced impact of the Aleutian Low on increasing the Central Pacific ENSO in recent decades. *NPJ Clim Atmos Sci* 6:29. <https://doi.org/10.1038/s41612-023-00350-1>
- Cheng X, Chen SF, Chen W, Hu P (2023) Observed impact of the Arctic Oscillation in boreal spring on the Indian Ocean Dipole in the following autumn and possible physical processes. *Clim Dyn*. <https://doi.org/10.1007/s00382-022-06616-3>
- Cherry S (1996) Singular value decomposition analysis and canonical correlation analysis. *J Clim* 9:2003–2009. [https://doi.org/10.1175/1520-0442\(1996\)009<2003:SVDAAC.2.0.CO;2](https://doi.org/10.1175/1520-0442(1996)009<2003:SVDAAC.2.0.CO;2)
- Chiang JCH, Vimont DJ (2004) Analogous Pacific and Atlantic meridional modes of tropical atmosphere–ocean variability. *J Clim* 17:4143–4158. <https://doi.org/10.1175/JCLI4953.1>
- Ding RQ, Li JP, Tseng YH, Sun C, Xie F (2017) Joint impact of North and South Pacific extratropical atmospheric variability on the onset of ENSO events. *J Geophys Res* 122:279–298
- Ding RQ, Tseng YH, Di Lorenzo E, Shi L, Li J, Yu JY, Wang CZ, Sun C, Luo JJ, Ha KJ, Hu ZZ, Li FF (2022) Multi-year El Niño events tied to the North Pacific Oscillation. *Nat Commun* 13:3871
- Du Y, Cai WJ, Wu YL (2013) A new type of the Indian Ocean Dipole since the mid-1970s. *J Clim* 26:959–972
- Duchon CE (1979) Lanczos filtering in one and two dimensions. *J Appl Meteorol Climatol* 18:1016–1022. [https://doi.org/10.1175/1520-0450\(1979\)018](https://doi.org/10.1175/1520-0450(1979)018)
- Fan L, Liu Q, Wang C, Guo F (2017) Indian Ocean dipole modes associated with different types of ENSO development. *J Clim* 30:2233–2249. <https://doi.org/10.1175/jcli-d-16-0426.1>
- Fan HJ, Huang BH, Yang S, Dong W (2021) Influence of the Pacific meridional mode on ENSO evolution and predictability: asymmetric modulation and ocean preconditioning. *J Clim* 34:1881–1901. <https://doi.org/10.1175/JCLI-D-20-0109.1>
- Fischer AS, Terray P, Guilyardi E, Gualdi S, Delecluse P (2005) Two independent triggers for the Indian Ocean dipole/zonal mode in a coupled GCM. *J Clim* 18:3428–3449. <https://doi.org/10.1175/JCLI3478.1>
- Francis PA, Gadgil S, Vinayachandran PN (2007) Triggering of the positive Indian Ocean dipole events by severe cyclones over the Bay of Bengal. *Tellus Ser 59A*(4):461–475. <https://doi.org/10.1111/j.1600-0870.2007.00254.x>
- Gill AE (1980) Some simple solutions for heat-induced tropical circulation. *Q J R Meteorol Soc* 106:447–462. <https://doi.org/10.1002/qj.49710644905>
- Graham FS, Brown JN, Langlais C (2014) Effectiveness of the Bjerknes stability index in representing ocean dynamics. *Clim Dyn* 43:2399–2414. <https://doi.org/10.1007/s00382-014-2062-3>
- Guan C, Wang X, Yang H (2023) Understanding the development of the 2018/19 Central Pacific El Niño. *Adv Atmos Sci* 40:177–185. <https://doi.org/10.1007/s00376-022-1410-1>
- Ham Y, Choi J, Kug JS (2017) The weakening of the ENSO–Indian Ocean Dipole (IOD) coupling strength in recent decades. *Clim Dyn* 49:249–261
- Hu P, Chen W, Chen SF et al (2021) Impact of the March Arctic Oscillation on the South China Sea summer monsoon onset. *Int J Climatol* 41:E3239–E3248. <https://doi.org/10.1002/joc.6920>
- Huang BH, Shukla J (2007) Mechanisms for the interannual variability in the tropical Indian Ocean. Part II: regional processes. *J Clim* 20:2937–2960. <https://doi.org/10.1175/Jcli4169.1>
- Huang G, Hu K, Xie S-P (2010) Strengthening of tropical Indian ocean teleconnection to the Northwest Pacific since the Mid-1970s: an atmospheric GCM study. *J Clim* 23:5294–5304
- Huang B et al (2017) Extended reconstructed sea surface temperature, Version 5 (ERSSTv5): upgrades, validations, and inter-comparisons. *J Clim* 30:8179–8205. <https://doi.org/10.1175/jcli-d-16-0836.1>
- Huang Z, Zhang WJ, Liu C, Stuecker MF (2022) Extreme Indian Ocean dipole events associated with El Niño and Madden-Julian oscillation. *Clim Dyn*. <https://doi.org/10.1007/s00382-022-06190-8>
- Izumo T, Vialard J, Lengaigne M et al (2010) Influence of the state of the Indian Ocean Dipole on the following years El Niño. *Nat Geosci* 3:168–172
- Izumo T, Lengaigne M, Vialard J et al (2014) Influence of Indian Ocean Dipole and Pacific recharge on following year’s El Niño: interdecadal robustness. *Clim Dyn* 42:291–310
- Jiang JL, Liu YM, Mao JY, Li JP, Zhao SW, Yu YQ (2022) Three types of positive Indian Ocean dipoles and their relationships with the South Asian summer monsoon. *J Clim* 35(1):405–424. <https://doi.org/10.1175/JCLI-D-21-0089.1>
- Kajikawa Y, Yasunari T, Kawamura R (2003) The role of the local Hadley circulation over the western Pacific on the zonally asymmetric anomalies over the Indian Ocean. *J Meteorol Soc Jpn* 81:259–276. <https://doi.org/10.2151/jmsj.81.259>
- Kalnay E et al (1996) The NCEP/NCAR 40-year reanalysis project. *Bull Am Meteorol Soc* 77:437–472

- Krishnaswamy J, Vaidyanathan S, Rajagopalan B (2015) Non-stationary and non-linear influence of ENSO and Indian Ocean Dipole on the variability of Indian monsoon rainfall and extreme rain events. *Clim Dyn* 45:175–184. <https://doi.org/10.1007/s00382-014-2288-0>
- Larson SM, Kirtman BP (2014) The Pacific meridional mode as an ENSO precursor and predictor in the North American Multimodel Ensemble. *J Clim* 27:7018–7032. <https://doi.org/10.1175/JCLI-D-14-00055.1>
- Lee SK, Lopez H, Foltz GR et al (2022) Java-Sumatra Niño/Niña and its impact on regional rainfall variability. *J Clim* 35(13):4291–4308. <https://doi.org/10.1175/jcli-d-21-0616.1>
- Li T, Wang B, Chang CP et al (2003) A theory for the Indian Ocean dipole-zonal mode. *J Atmos Sci* 60:2119–2135. [https://doi.org/10.1175/1520-0469\(2003\)060%3c2119:Atftio%3e2.0.Co;2](https://doi.org/10.1175/1520-0469(2003)060%3c2119:Atftio%3e2.0.Co;2)
- Liang XS (2014) Unraveling the cause-effect relation between time series. *Phys Rev E* 90:052150. <https://doi.org/10.1103/PhysRevE.90.052150>
- Lin CY, Yu JY, Hsu HH (2015) CMIP5 model simulations of the Pacific meridional mode and its connection to the two types of ENSO. *Int J Climatol* 35:2352–2358. <https://doi.org/10.1002/joc.4130>
- Liu HF, Tang YM, Chen DK, Lian T (2017) Predictability of the Indian Ocean Dipole in the coupled models. *Clim Dyn* 48:2005–2024
- Liu C, Zhang W, Stuecker MF, Jin F (2019) Pacific meridional mode-western north pacific tropical cyclone linkage explained by tropical pacific quasi-decadal variability. *Geophys Res Lett* 46:13346–13354. <https://doi.org/10.1029/2019GL085340>
- Lu B, Ren HL, Scaife A, Wu J, Dunstone N, Smith D, Wan J, Eade R, MacLachlan C, Gordon M (2018) An extreme negative Indian Ocean Dipole event in 2016: dynamics and predictability. *Clim Dyn* 51:89–100
- Luo JJ, Zhang RC, Behera SK, Masumoto Y, Jin FF, Lukas R, Yamagata T (2010) Interaction between El Niño and extreme Indian Ocean dipole. *J Clim* 23:726–742
- Min Q, Su J, Zhang R (2017) Impact of the South and North Pacific meridional modes on the El Niño-Southern Oscillation: observational analysis and comparison. *J Clim* 30:1705–1720. <https://doi.org/10.1175/JCLI-D-16-0063.1>
- Qiu Y, Cai W, Guo X, Ng B (2014) The asymmetric influence of the positive and negative IOD events on China's rainfall. *Sci Rep* 4:1–6
- Qu T (2003) Mixed layer heat balance in the Western North Pacific. *J Geophys Res* 108(C7):3242. <https://doi.org/10.1029/2002JC001536>
- Richter I, Stuecker MF, Takahashi N, Schneider N (2022) Disentangling the North Pacific Meridional Mode from tropical Pacific variability. *NPJ Clim Atmos Sci* 5:94. <https://doi.org/10.1038/s41612-022-00317-8>
- Roxy M, Gualdi S, Drbohlav HKL, Navarra A (2011) Seasonality in the relationship between El Niño and Indian Ocean dipole. *Clim Dyn* 37(1):221–236. <https://doi.org/10.1007/s00382-010-0876-1>
- Saji NH, Goswami BN, Vinayachandran PN, Yamagata T (1999) A dipole mode in the tropical Indian Ocean. *Nature* 401:360–363. <https://doi.org/10.1038/43854>
- Santoso A, Sen Gupta A, England MH (2010) Genesis of Indian Ocean mixed layer temperature anomalies: a heat budget analysis. *J Clim* 23(20):5375–5403. <https://doi.org/10.1175/2010JCLI3072.1>
- Schiller A, Ridgway KR (2013) Seasonal mixed layer dynamics in an eddy-resolving Ocean circulation model. *J Geophys Res* 118:1–19. <https://doi.org/10.1002/jgrc.20250>
- Song Q, Gordon AL (2004) Significance of the vertical profile of the Indonesian throughflow transport to the Indian Ocean. *Geophys Res Lett* 31:L16307. <https://doi.org/10.1029/2004GL020360>
- Strnad FM, Schlör J, Fröhlich C, Goswami B (2022) Teleconnection patterns of different El Niño types revealed by climate network curvature. *Geophys Res Lett* 49:e2022GL098571. <https://doi.org/10.1029/2022GL098571>
- Tao YQ, Qiu CH, Zhong WX, Zhang GL, Wang L (2023) Distinctive characteristics and dynamics of the summer and autumn Indian Ocean dipole events. *Clim Dyn*. <https://doi.org/10.1007/s00382-023-06942-0>
- Terray P, Chauvin F, Douville H (2007) Impact of southeast Indian Ocean Sea surface temperature anomalies on monsoon-ENSO-dipole variability in a coupled ocean-atmosphere model. *Clim Dyn* 28(6):553–580. <https://doi.org/10.1007/s00382-006-0192-y>
- Tozuka T, Endo S, Yamagata T (2016) Anomalous Walker circulations associated with two flavors of the Indian Ocean Dipole. *Geophys Res Lett* 43:5378–5384. <https://doi.org/10.1002/2016GL068639>
- Trenberth KE (1997) The definition of El Niño. *Bull Am Meteorol Soc* 78:2771–2777. [https://doi.org/10.1175/1520-0477\(1997\)078%3c2771:Tdoeno%3e2.0.Co;2](https://doi.org/10.1175/1520-0477(1997)078%3c2771:Tdoeno%3e2.0.Co;2)
- Vijith V, Vinayachandran PN, Webber BGM (2020) Closing the sea surface mixed layer temperature budget from in situ observations alone: operation advection during BoBBLE. *Sci Rep* 10:7062. <https://doi.org/10.1038/s41598-020-63320-0>
- Vimont DJ, Wallace JM, Battisti DS (2003) The seasonal footprinting mechanism in the Pacific: implications for ENSO. *J Clim* 16:2668–2675
- Von Storch H, Zwiers FZ (1999) Statistical analysis in climate research. Cambridge University Press, Cambridge, p 484. <https://doi.org/10.1017/CBO9780511612336>
- Wahiduzzaman M, Cheung K, Luo J, Bhaskaran P, Tang S, Yuan C (2022) Impact assessment of Indian Ocean Dipole on the North Indian Ocean tropical cyclone prediction using a Statistical model. *Clim Dyn* 58:1275–1292. <https://doi.org/10.1007/s00382-021-05960-0>
- Wallace JM, Smith C, Bretherton CS (1992) Singular value decomposition of wintertime sea surface temperature and 500-mb height anomalies. *J Clim* 5:561–576. [https://doi.org/10.1175/15200442\(1992\)005<0561:SVDOWS.2.0.CO;2](https://doi.org/10.1175/15200442(1992)005<0561:SVDOWS.2.0.CO;2)
- Wang C (2019) Three-ocean interactions and climate variability: a review and perspective. *Clim Dyn* 53:18. <https://doi.org/10.1007/s00382-019-04930-x>
- Wang CZ, Wang X (2013) Classifying El Niño Modoki I and II by different impacts on rainfall in Southern China and typhoon tracks. *J Clim* 26:1322–1338. <https://doi.org/10.1175/JCLI-D-12-00107.1>
- Wang X, Wang CZ (2014) Different impacts of various El Niño events on the Indian Ocean Dipole. *Clim Dyn* 42:991–1005. <https://doi.org/10.1007/s00382-013-1711-2>
- Wang C, Kucharski F, Barimalala R, Bracco A (2009) Teleconnections of the tropical Atlantic to the tropical Indian and Pacific Oceans: a review of recent findings. *Meteorol Z* 18:445–454. <https://doi.org/10.1127/0941-2948/2009/0394>
- Wang H, Murtugudde R, Kumar A (2016) Evolution of Indian Ocean dipole and its forcing mechanisms in the absence of ENSO. *Clim Dyn* 47:2481–2500
- Wang X, Tan W, Wang CZ (2018) A new index for identifying different types of El Niño Modoki events. *Clim Dyn* 50:2753–2765. <https://doi.org/10.1007/s00382-017-3769-8>
- Wang X, Guan C, Huang RX (2019) The roles of tropical and subtropical wind stress anomalies in the El Niño Modoki onset. *Clim Dyn* 52:6585–6597. <https://doi.org/10.1007/s00382-018-4534-3>
- Webster PJ, Moore AM, Loschnigg JP, Leben RR (1999) Coupled ocean-atmosphere dynamics in the Indian Ocean during 1997–98. *Nature* 401:356–360. <https://doi.org/10.1038/43848>

- Xie P, Arkin PA (1996) Analyses of global monthly precipitation using gauge observations, satellite estimates, and numerical model predictions. *J Clim* 9:840–858
- Xie SP, Philander SGH (1994) A coupled ocean-atmosphere model of relevance to the ITCZ in the eastern Pacific. *Tellus Ser A Dyn Meteorol Oceanol* 46:340–350. <https://doi.org/10.1034/j.1600-0870.1994.t01-1-00001.x>
- Xie SP, Annamalai H, Schott FA, McCreary JP (2002) Structure and mechanisms of South Indian Ocean climate variability. *J Clim* 15:864–878. [https://doi.org/10.1175/1520-0442\(2002\)015%3c0864:SAMOSI%3e2.0.CO;2](https://doi.org/10.1175/1520-0442(2002)015%3c0864:SAMOSI%3e2.0.CO;2)
- Yamagata T, Behera SK, Luo JJ (2004) Coupled ocean-atmosphere variability in the tropical Indian ocean. *Geophys Monogr Ser* 147:189–211
- Yang Y et al (2015) Seasonality and predictability of the Indian Ocean Dipole mode: ENSO forcing and internal variability. *J Clim* 28:8021–8036. <https://doi.org/10.1175/JCLI-D-15-0078.1>
- Yeh S, Wang X, Wang CZ, Dewitte B (2015) On the relationship between the North Pacific climate variability and the Central Pacific El Niño. *J Clim* 28:663–677. <https://doi.org/10.1175/JCLI-D-14-00137.1>
- Yu JY, Kim ST (2010) Three evolution patterns of Central-Pacific El Niño. *Geophys Res Lett* 37:L08706. <https://doi.org/10.1029/2010GL042810>
- Yu JY, Kao HY, Lee T (2010) Subtropics-related interannual sea surface temperature variability in the central equatorial Pacific. *J Clim* 23:2869–2884. <https://doi.org/10.1175/2010JCLI3171.1>
- Zhang W, Wang Y, Jin F-F, Stuecker MF, Turner AG (2015) Impact of different El Niño types on the El Niño/IOD relationship. *Geophys Res Lett* 42:8570–8576. <https://doi.org/10.1029/2020GL090323>
- Zhang YZ et al (2018) Impact of the South China Sea Summer Monsoon on the Indian Ocean Dipole. *J Clim* 31:6557–6573. <https://doi.org/10.1175/jcli-d-17-0815.1>
- Zhang C, Luo JJ, Li S (2019) Impacts of tropical Indian and Atlantic Ocean warming on the occurrence of the 2017/2018 La Niña. *Geophys Res Lett* 46:3435–3445. <https://doi.org/10.1029/2019GL082280>
- Zhang G, Wang X, Xie Q, Chen J, Chen S (2022a) Strengthening impacts of spring sea surface temperature in the north tropical Atlantic on Indian Ocean dipole after the mid-1980s. *Clim Dyn*. <https://doi.org/10.1007/s00382-021-06128-6>
- Zhang L, Shi RZ, Fraedrich K, Zhu X (2022b) Enhanced joint effects of ENSO and IOD on Southeast China winter precipitation after 1980s. *Clim Dyn* 58:277–292
- Zhang Y, Zhou W, Wang X, Chen S, Chen J, Li S (2022c) Indian Ocean Dipole and ENSO's mechanistic importance in modulating the ensuing-summer precipitation over Eastern China. *NPJ Clim Atmos Sci* 5:48. <https://doi.org/10.1038/s41612-022-00271-5>
- Zhang YZ, Li JP, Diao YN, Hou ZL, Liu T, Zuo B (2023) Energetic connection between the South China Sea summer monsoon and Indian Ocean dipole from the perspective of perturbation potential energy. *Clim Dyn*. <https://doi.org/10.1007/s00382-023-06693-y>
- Zheng YQ, Chen W, Chen SF, Yao SL, Cheng CL (2021a) Asymmetric impact of the boreal spring Pacific Meridional Mode on the following winter El Niño-Southern Oscillation. *Int J Climatol* 41:3523–3538
- Zheng YQ, Chen W, Chen SF (2021b) Intermodel spread in the impact of the springtime Pacific meridional mode on following-winter ENSO tied to simulation of the ITCZ in CMIP5/CMIP6. *Geophys Res Lett* 48:e2021GL093945. <https://doi.org/10.1029/2021GL093945>
- Zheng YQ, Chen SF, Chen W, Yu B (2023) A continuing increase of the impact of the Spring North Pacific meridional mode on the following Winter El Niño and Southern Oscillation. *J Clim* 36(2):585–602

Publisher's Note Springer Nature remains neutral with regard to jurisdictional claims in published maps and institutional affiliations.

Springer Nature or its licensor (e.g. a society or other partner) holds exclusive rights to this article under a publishing agreement with the author(s) or other rightsholder(s); author self-archiving of the accepted manuscript version of this article is solely governed by the terms of such publishing agreement and applicable law.